

ACTA

*Francis Gyakwaa*

APPLICATION OF RAMAN  
SPECTROSCOPY FOR  
THE CHARACTERISATION OF  
SYNTHETIC NON-METALLIC  
INCLUSIONS FOUND IN AL-  
KILLED CALCIUM TREATED  
STEELS

UNIVERSITY OF OULU GRADUATE SCHOOL;  
UNIVERSITY OF OULU,  
FACULTY OF TECHNOLOGY





ACTA UNIVERSITATIS OULUENSIS  
C Technica 762

*FRANCIS GYAKWAA*

**APPLICATION OF RAMAN  
SPECTROSCOPY FOR  
THE CHARACTERISATION OF  
SYNTHETIC NON-METALLIC  
INCLUSIONS FOUND IN AL-KILLED  
CALCIUM TREATED STEELS**

Academic dissertation to be presented with the assent of  
the Doctoral Training Committee of Technology and  
Natural Sciences of the University of Oulu for public  
defence in Auditorium AT117, Linnanmaa, on 20  
November 2020, at 12 noon

UNIVERSITY OF OULU, OULU 2020

Copyright © 2020  
Acta Univ. Oul. C 762, 2020

Supervised by  
Professor Timo Fabritius  
Professor Marko Huttula  
Doctor Matti Aula

Reviewed by  
Docent Andrey Karasev  
Associate Professor Silvia Barella

Opponent  
Associate Professor Susanne K. Michelic

ISBN 978-952-62-2728-3 (Paperback)  
ISBN 978-952-62-2729-0 (PDF)

ISSN 0355-3213 (Printed)  
ISSN 1796-2226 (Online)

Cover Design  
Raimo Ahonen

PUNAMUSTA  
TAMPERE 2020

**Gyakwaa, Francis, Application of Raman spectroscopy for the characterisation of synthetic non-metallic inclusions found in Al-killed calcium treated steels.**

University of Oulu Graduate School; University of Oulu, Faculty of Technology

*Acta Univ. Oul. C 762, 2020*

University of Oulu, P.O. Box 8000, FI-90014 University of Oulu, Finland

***Abstract***

Non-metallic inclusions form an essential parameter for assessing steel cleanliness. The chemical composition of the inclusions and content found in the steel matrix can be detrimental to both the steelmaking process and steel properties. Therefore, a characterisation technique that has features such as an improved duration for sample preparation, a non-destructive and relatively fast result analysis is of high interest to both researchers and steelmakers.

The main objective of this study is to use Raman spectroscopy as an analytical technique to characterise synthetic non-metallic inclusions mostly associated with aluminium-killed calcium treated steels. The work first examines the possibility of estimating individual phase content for synthetic inclusion mixtures consisting of CA, C12A7, C3A, MgO.Al<sub>2</sub>O<sub>3</sub> and CaS phases by using Raman spectroscopy. Observations made from the Raman spectra measured provide qualitative information for the specific phases present in the samples. The results from the study using calibration models are satisfactory in quantifying the specific phase content present in the sample mixtures based on the Raman spectral data.

Additionally, this study investigates the potential use of Raman spectroscopy as a characterisation technique for inclusion evolution studies and to predict the liquidus region within a CaO–Al<sub>2</sub>O<sub>3</sub> binary system under steelmaking temperatures. This is done by using different synthetic inclusion phases to generate the sample matrix that has varying phase content for possible inclusion evolution routes. The experimental measurements performed with Raman spectroscopy prove to have a relatively short duration for sample preparation, fast results, and the synthetic inclusion phases can be distinguished based on their characteristic Raman bands features. Consequently, this study shows that Raman spectroscopy can potentially be used as an analytical technique for inclusion studies in steel samples since the steel matrix is Raman inactive.

*Keywords:* characterisation, non-metallic inclusion, Raman spectroscopy, steel



# **Gyakwaa, Francis, Raman-spektroskopian käyttäminen synteettisten ei-metallisten sulkeumien karakterisointiin alumiinitiiivistetyissä kalsiumkäsitellyissä teräksissä.**

Oulun yliopiston tutkijakoulu; Oulun yliopisto, Teknillinen tiedekunta

*Acta Univ. Oul. C 762, 2020*

Oulun yliopisto, PL 8000, 90014 Oulun yliopisto

## ***Tiivistelmä***

Ei-metalliset sulkeumat ovat tärkeä teräksen puhtauden arviointikriteeri. Sulkeumien kemiallinen koostumus, koko ja muoto teräsmatriisissa voivat vaikuttaa haitallisesti teräksen valmistusprosessiin ja teräksen ominaisuuksiin. Karakterisointitekniikka, joka lyhentää näytteiden käsittelyaikaa ja mahdollistaa ainetta rikkomattoman testauksen ja tulosten suhteellisen nopean analysoinnin, on erittäin kiinnostava sekä tutkijoille että teräsvalmistajille.

Tämän tutkimuksen päätaavoitteena on käyttää Raman-spektroskopiaa analyysitekniikkana synteettisten ei-metallisten sulkeumien karakterisoimiseksi alumiinitiiivistetyissä ja kalsiumkäsitellyissä teräksissä. Tutkimuksessa tutkitaan ensin mahdollisuutta määrittää yksittäisen faasin kemiallinen koostumus synteettisissä inkluusioseoksissa, joissa on CA, C12A7, C3A ja MgO-Al<sub>2</sub>O<sub>3</sub>, sekä CaS-faaseja käyttämällä Raman-spektroskopiaa. Mitatusta Raman-spektristä tehdyt havainnot osoittavat, että näyteseosten koostumus on määritettävissä tutkituille näytteille. Kalibrointimalleja käyttämällä saadut tulokset osoittavat, että faasiosuuksien määrittäminen onnistuu riittäväällä tarkkuudella Raman-spektridatan avulla.

Lisäksi tutkimuksessa tutkitaan Raman-spektroskopian käyttöpotentiaalia karakterisointitekniikkana sulkeumien analysoinnissa ja likvidusalueen laajuuden ennakoinnissa binäärissä CaO–Al<sub>2</sub>O<sub>3</sub> systeemissä teräksenvalmistuslämpötiloissa. Tutkimuksessa on luotu erilaisia synteettisiä monikomponenttisulkeumia käyttämällä näytematriisi, joka sisältää laajasti eri faasikoostumuksia, sulkeumien mahdollisten kehitysreittien tutkimiseksi. Raman-spektroskopiaa hyödyntämällä tehdyissä testeissä on osoittautunut, että näytteiden valmistelu vaatii aiempaa vähemmän aikaa, tulokset saadaan aiempaa nopeammin ja synteettisten sulkeumien koostumus voidaan identifioida faaseille ominaisten Raman-sidosten perusteella. Tutkimus osoittaa siten, että Raman-spektroskopiaa voidaan hyödyntää analyysitekniikkana teräsnäytteiden sulkeumatutkimuksissa, koska teräsmatriisi on passiivinen Raman-säteilylle.

*Asiasanat:* ei-metallinen sulkeuma, karakterisointi, Raman-spektroskopia, teräs



## Acknowledgements

The research for this thesis was conducted between 2017 and 2020 at the Process Metallurgy Research Unit at the University of Oulu, Finland. The work forms part of the I4Future doctoral programme - Imaging for the Future: *Novel Imaging and Characterization Methods in Bio, Medical and Environmental Research and Technology Innovations*; received funding from by European Union's Horizon 2020 research and innovation programme (under the Marie Skłodowska-Curie grant agreement no. 713606) and Academy of Finland Profilation project (Academy of Finland, no. 311934).

I would like to thank my supervisors Prof. Timo Fabritius, Prof. Marko Huttula and Dr. Matti Aula, for their guidance and encouragement in performing the research. I would like to extend my special thanks to Mr. Riku Mattila and Mr. Tommi Kokkonen for their unrelenting support during my entire doctoral studies. I would like to acknowledge Adjunct Professor (Docent) Satu Ojala in Chemical and Environmental Engineering Unit, the University of Oulu for the valuable lessons on the primary equipment used for this research. To the entirety of the process Metallurgy Research Unit staffs, thank you for support and collaboration. I would thank Mikko Jokinen and the entire staffs of LUXMET Ltd for hosting me for my secondment. I would also like to thank staffs of Timegate Instrument Ltd, Finland for their technical support.

Pre-examiners, Docent Andrey Karasev and Associate professor Silvia Barella are acknowledged for their valuable comments concerning this thesis.

Finally, I would like to thank my parents, siblings, friends and especially to my daughters Isabella and Annabella, and my dear wife Veronica, for their encouragement and unrelenting supporting me to focus and complete my doctoral studies. Special thanks to Pete Miikkola and Katariina Miikkola for their support. I would also like to thank my colleagues in I4Future doctoral programme, the entire team of the I4Future doctoral programme and the Ghanaian community in Oulu.

September 1, 2020

Francis Gyakwaa



## Abbreviations and symbols

CMOS	Complementary Metal Oxide Semiconductor
O <sub>toc</sub>	Total oxygen content
MAE	Mean Absolute Error
MLR	Multiple Linear Regression
PCA	Principal Component Analysis
PDA	Pulse Discrimination Analysis
PLS	Partial Least Squares
R <sup>2</sup>	Coefficient of determination
RMSE	Root Mean Standard Error
RMSEC	Root Mean Standard Error in Calibration
RMSCV	Root Mean Standard Error in Cross-Validation
RMSEP	Root Mean Square Error of Prediction
RPD	Ratio of Prediction to Deviation
SD	Standard Deviation
S <sub>i</sub>	Relative stabilities
SPA	Successive Projection Algorithm
SPAD	Single-Photon Avalanche Diode
SNR	Signal-to-Noise Ratio
SNV	Standard Normal Variate
wt%	Weight percent
XRD	X-ray diffraction
XRF	X-ray fluorescence

### Chemical elements and compounds

Al	Aluminium
Ca	Calcium
Cu	Copper
O	Oxygen
Mg	Magnesium
Mn	Manganese
S	Sulfur
Si	Silicon
Ti	Titanium
Zr	Zirconium
Al <sub>2</sub> O <sub>3</sub>	Aluminium oxide

CaO	Calcium oxide
CaS	Calcium sulphide
MgO	Magnesium oxide
MA	Magnesium aluminate spinel ( $\text{MgO}\cdot\text{Al}_2\text{O}_3$ )
CA	Monocalcium aluminate ( $\text{CaO}\cdot\text{Al}_2\text{O}_3$ )
CA2	Calcium di-aluminate
CA6	calcium hexa-aluminate
C3A	Tricalcium aluminate, ( $3\text{CaO}\cdot\text{Al}_2\text{O}_3$ )
C12A7	Mayenite or dodeca-calcium hepta-aluminate ( $12\text{CaO}\cdot 7\text{Al}_2\text{O}_3$ )

Units

$\text{cm}^{-1}$	Reciprocal centimetres
$^{\circ}\text{C}$	Degree Celsius
mA	Milliamperes
nm	Nanometre
kHz	Kilohertz
kV	Kilovolt
kW	Kilowatt

## List of original publications

This thesis is based on the following publications, which are referred throughout the text by their Roman numerals (I–V):

- I Gyakwaa, F., Aula, M., Alatarvas, T., Vuolio, T., Huttula, M., & Fabritius, T. (2019). Applicability of time-gated Raman spectroscopy in the characterisation of calcium-aluminate inclusions. *ISIJ International*, *59*(10), 1846–1852. doi: /10.2355/isijinternational.ISIJINT-2019-122
- II Gyakwaa, F., Aula, M., Alatarvas, T., Vuolio, T., Shu, Q., Huttula, M., & Fabritius, T. (2020). Characterisation of binary phase mixtures of magnesium-aluminate spinel and calcium-aluminates using time-gated Raman spectroscopy. *ISIJ International*, *60*(5), 988–997. doi: 10.2355/isijinternational.ISIJINT-2019-576
- III Gyakwaa, F., Aula, M., Vuolio, T., Alatarvas, T., Shu, Q., Huttula, M., & Fabritius, T. (2020). Characterisation of multiphase mixtures of calcium aluminates and magnesium aluminate spinel using time-gated Raman spectroscopy. *Steel Research International*, *91*(8), 2000084. doi: 10.1002/srin.202000084
- IV Gyakwaa, F., Aula, M., Alatarvas, T., Vuolio, T., Shu, Q., Huttula, M., & Fabritius, T. (2020). Application of Raman spectroscopy for characterising synthetic non-metallic inclusions consisting of calcium sulphide and oxides. *Applied Sciences*, *10*(6), 2113. doi:10.3390/app10062113
- V Gyakwaa, F., Aula, M., Alatarvas, T., Shu, Q., Huttula, M., & Fabritius, T. (2020). Quantification of synthetic nonmetallic inclusion multiphase mixtures from a CaO–Al<sub>2</sub>O<sub>3</sub>–MgO–CaS system using time-gated Raman spectroscopy. *Steel Research International*, 2000322. doi: 10.1002/srin.202000322

All the papers for this doctoral dissertation were written by the author with the assistance of co-authors. The author's main responsibilities involved conducting experimental measurements, data collection, part of the calibration models for the data treatment, and reporting the results. The discussions section in the papers was written by the author with the support of the co-authors.



# Contents

<b>Abstract</b>	
<b>Tiivistelmä</b>	
<b>Acknowledgements</b>	<b>7</b>
<b>Abbreviations and symbols</b>	<b>9</b>
<b>List of original publications</b>	<b>11</b>
<b>Contents</b>	<b>13</b>
<b>1 Introduction</b>	<b>15</b>
1.1 Steel cleanliness and assessment.....	15
1.2 Objectives and scope of the study .....	17
<b>2 Theoretical background</b>	<b>19</b>
2.1 Non-metallic inclusions .....	19
2.1.1 Calcium treatment .....	20
2.1.2 Inclusion formation and evolution process.....	21
2.1.3 Classification of inclusions.....	22
2.2 Characterisation and assessment techniques .....	24
2.3 Brief background of Raman spectroscopy .....	24
2.3.1 Applications of Raman spectroscopy .....	28
2.3.2 Limitations of Raman spectroscopy .....	29
2.3.3 Raman spectroscopy instrumentation.....	30
2.4 Calibration model identification and multivariate analysis.....	31
2.4.1 Model selection .....	31
2.4.2 Multivariate analysis .....	33
<b>3 Experiment</b>	<b>37</b>
3.1 Description of the experimental procedure .....	37
3.1.1 Preparation of synthetic inclusion samples .....	37
3.1.2 Sample matrix.....	38
3.2 Verification of synthetic inclusion samples prepared.....	41
3.2.1 XRD and XRF .....	41
3.3 Raman spectroscopic measurement .....	42
<b>4 Results and discussion</b>	<b>45</b>
4.1 Identification of the sample's composition using XRF and XRD.....	45
4.2 Identifiable Raman bands for synthetic inclusion phases .....	49
4.2.1 Raman spectral observations based on the phases studied .....	51
4.3 Phase quantification based on Raman spectral data.....	55
4.3.1 Calcium aluminate phases .....	55

4.3.2	Calcium aluminate – MgO·Al <sub>2</sub> O <sub>3</sub> sample mixtures.....	57
4.3.3	Calcium aluminate – MgO·Al <sub>2</sub> O <sub>3</sub> – CaS system.....	60
4.4	Prospect for application of Raman spectroscopy for steel samples studies.....	65
4.4.1	Liquidus region prediction.....	65
4.4.2	Predicting evolution and formation routes for non-metallic inclusions based on Raman spectroscopy.....	67
<b>5</b>	<b>Conclusions and future work</b>	<b>69</b>
5.1	Conclusions.....	69
5.2	Future work.....	71
	<b>List of references</b>	<b>73</b>
	<b>Original publications</b>	<b>79</b>

# 1 Introduction

## 1.1 Steel cleanliness and assessment

The end-users of steel products continue to demand high-quality steels from steelmaking industries. Therefore, steelmakers work towards steel cleanliness to meet this demand through the utilisation of controlled and improved production practices throughout the steelmaking process as a necessity for high-quality steel. Steel cleanliness also contributes to the competitiveness and sustainability of the steel industry. Generally, the level of steel cleanliness could briefly be explained as being the content of harmful elements, such as oxygen, carbon, sulphur and phosphorus (Kießling, 1980; Holappa & Helle, 1995; Zhang & Thomas, 2003).

Steel cleanliness could also be further described as being the content or nature of non-metallic inclusions found in the steel matrix. Depending on the type and content of non-metallic inclusions, it can be considered detrimental to the steelmaking process, the final steel product and quality. Examples of such inclusions are oxides, sulphides and nitrides. Deterioration of the surface quality of steel products and potential nozzle clogging during the steelmaking process are some of the demerits associated with non-metallic inclusions (Xu, Liu, He & Pang, 2018; Zhang & Thomas, 2003).

For high-performance steels, non-metallic inclusions could have an impact on the steel microstructure and structural properties in the final steel product. A non-metallic inclusion originates from various sources that depend on physical and chemical interactions between the molten steel, refractories, slag or the gas phases, as well as those processes used for controlling the total oxygen content in the steel melt. To minimise the detrimental effect of inclusions and to enhance the quality of the final steel product, researchers and steelmakers continue to study the mechanisms for the formation of non-metallic inclusions, chemical interaction, and potential separation during the steelmaking process.

Another essential aspect to consider for steel cleanliness is the use of characterisation techniques for assessing non-metallic inclusions. The assessment could provide detailed information such as composition, size, spatial distribution, and morphology of inclusions. In addition, the characterisation of inclusion presents an opportunity for the formation and evolution process for the inclusions to be analysed, and for appropriate measures to be adopted for controlling and monitoring purposes. Review literature conducted by Zhang and Thomas (2003)

provides a list of characterisation techniques, such as scanning electron microscopy (SEM), optical emission spectrometry with pulse discrimination analysis (OES-PDA) and among others, detailing the merit and demerits for using these methods to evaluate steel cleanliness.

The interest in having analytical or characterisation techniques that provide relatively fast, non-destructive, easy or a short duration of time for sample preparation to assess inclusions could potentially improve and help in controlling and for monitoring during the steelmaking process. Consequently, an analytical technique with such features could relatively assist for routine measurements, and possibly be used for in situ or online characterisation of non-metallic inclusions. One possibility is Raman spectroscopy, which is a well-known vibrational and versatile spectroscopic instrument with features such as the non-contact and relatively non-destructive technique used for studying the vibrational and rotational modes of excited molecules in a material.

Raman active materials can be measured non-destructively, relatively fast, and with little or a short duration of time for sample preparation using Raman spectroscopy. Ferraro, Nakamoto and Brown (2003) suggest that when laser light interacts with molecular vibrations in Raman active material, a change is triggered in the energy from the scattered photons. The shift or change in energy resulting from the laser interaction with the material is a characteristic function of the vibrational modes of a molecule. The Raman spectrum obtained from the measured material or sample produces unique vibrational fingerprints for identifying the composition within the material or sample.

The use of Raman spectroscopy as a characterisation technique continues to contribute significantly to steelmaking research, such as for slag characterisation and structural analysis. Furthermore, synthetic non-metallic inclusions, such as some oxide and sulphides phases, have shown to be Raman active while the steel matrix is regarded as not Raman active. Additionally, it has been demonstrated from the studies conducted by Li and Hihara (2017) that oxide inclusions such as CA and CA<sub>2</sub> can be characterised in steel samples using Raman spectroscopy. Therefore, the use of Raman spectroscopy presents a potential tool that can be used for the identification and characterisation of a non-metallic inclusion and which meets the need for a more robust characterisation technique for inclusions studies.

## 1.2 Objectives and scope of the study

The main objective of this doctoral thesis is to examine the application of Raman spectroscopy for the identification and characterisation of synthetic non-metallic inclusions mainly associated with aluminium-killed and calcium-treated steels. The study is classified into four main tasks:

- The use of Raman spectroscopy to characterise the relatively low-melting calcium aluminate phase of C12A7 along with CA and C3A, and also to predict the liquidus region within a CaO–Al<sub>2</sub>O<sub>3</sub> binary system.
- The identification and characterisation of generally harmful synthetic non-metallic inclusions of MA spinel or CaS combined with a calcium aluminate phase (CA, C12A7 and C3A) sample mixture using Raman spectroscopy.
- The application of Raman spectroscopy combined with a multivariate technique to quantify a multiphase consisting of (CaO–Al<sub>2</sub>O<sub>3</sub>)–CaS–MA spinel synthetic inclusions.
- To demonstrate the prospect of using Raman spectroscopy for future steel sample non-metallic inclusion studies.

All the Papers I–V used for this study are presented with a schematic chart, as illustrated in Figure 1. A brief description of the focus and concept for each paper are shown below:

Paper I: Studies the characterisation of the fully modified liquid calcium aluminate phase of C12A7 and its interaction with the closest phase of CA and C3A to estimate the liquidus region within a CaO–Al<sub>2</sub>O<sub>3</sub> binary system using under steelmaking temperature Raman spectroscopy.

Papers II and III: These studies examine how to distinguish the detrimental MA spinel from the calcium aluminate phases of CA, C12A7 and C3A with Raman spectroscopy.

Paper IV: Synthetic duplex CaS-oxides are studied to demonstrate the possibility of using Raman spectroscopy to estimate the CaS content from binary samples, as presented in Figure 1.

Paper V: This study illustrates the application of Raman spectroscopy to quantify a generally complex synthetic inclusion consisting of MA spinel-calcium aluminate (CA, C12A7 and C3A)–CaS.

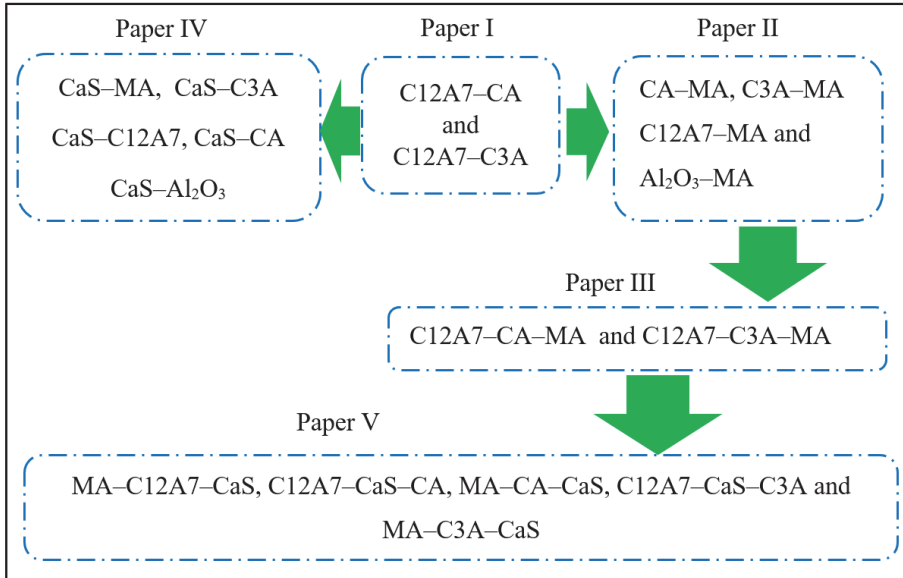


**Fig. 1. Synthetic non-metallic inclusion sample matrix for Papers I–V.**

The doctoral thesis first presents some literature research carried out concerning non-metallic inclusions and brief background information for Raman spectroscopy. The background literature research gives a general perspective for the studies that are related to a non-metallic inclusion, particularly for inclusions associated with Al-killed and calcium-treated steel. In addition, the background studies discuss the application and robustness of Raman spectroscopy as a characterisation technique. The experimental procedure for sample preparation and measurements are explained. As well as this, the results obtained based on the Raman spectral data are discussed. The conclusion and recommendation for future studies are finally presented.

## 2 Theoretical background

### 2.1 Non-metallic inclusions

In steelmaking processes, one of the initial potential detrimental parameters for the assessment of steel cleanliness is the level of the total oxygen content ( $O_{\text{toc}}$ ) in the molten steel (Cho & Suito, 1994). Studies conducted by Göransson and Jänsson (2001) suggest that high  $O_{\text{toc}}$  is undesirable and therefore, should be controlled to a minimum level in the steel melt. An oxygen removal process called a deoxidation process is commonly used to lower the dissolved or active oxygen content in the molten steel before cooling down and solidification. The deoxidation process can be accomplished by introducing elements such as aluminium (Zhang & Chou, 2015) or by using the Zr-Ti based deoxidising agent Si (Wu et al., 2016) in the ladle during tapping where it reacts with the dissolved oxygen present in the molten steel (Taguchi et al., 2005).

The most commonly used element as a deoxidiser in steel industries is aluminium (Al), because of its high deoxidation efficiency and potential cost factor (Fandrich, Lungen, & Wuppermann, 2008). According to Fandrich et al. (2008), a deoxidation process using Al helps in the reduction of oxygen activity in the molten steel to form oxide inclusions.

The effectiveness of the deoxidation process depends on how Al introduced into the molten steel during tapping is consumed. Based on studies conducted by Kawawa and Ohkubo (1968), Conejo and Hernández (2006), Holappa, (2014) and He, Chen, Guo, Shen and Wang (2015) some suggested ways in which Al consumption occurs during deoxidation process include:

- Aluminium reacting with the dissolved or active oxygen in the molten steel.
- The dissolution of Al in the molten steel to generate a reaction product of  $\text{Al}_2\text{O}_3$  that could be floated up to the top slag and partially retained in the steel melt as a solid  $\text{Al}_2\text{O}_3$  inclusion.
- The oxidation of Al caused by air entrainment or absorbed top slag.

The potential loss of aluminium resulting from oxygen picked up through air entrainment is considered negligible when the deoxidation process is managed and controlled well (Cho & Suito, 1994). The expectation for the deoxidation process is to have the reaction product ( $\text{Al}_2\text{O}_3$ ) floated from the steel melt up to the slag. However, a significant drawback associated with the Al deoxidation process identified by Cicutti, Madías and González (1997) and Sakata (2006) includes the

potential interruption of the casting process as a result of a solid  $\text{Al}_2\text{O}_3$  inclusion formed in the molten steel becoming attached to the inner wall of the immersion nozzle causing clogging.

Additionally, the presence of MgO in the molten steel can react with  $\text{Al}_2\text{O}_3$  to form a MA spinel inclusion. Potential sources of Mg can be attributable to refractories such as a MgO refractory according to Brabie (1996) and Deng, Zhu, and Sichen (2016). Though the deoxidation process can be successful in suppressing the total oxygen content in the steel melt, Park and Todoroki (2010) and Poirier (2015) suggest that the presence of solid  $\text{Al}_2\text{O}_3$  or the formation of  $\text{MgO}.\text{Al}_2\text{O}_3$  inclusions in the steel matrix can affect steel cleanliness.

### **2.1.1 Calcium treatment**

The detrimental  $\text{Al}_2\text{O}_3$  inclusion obtained from the deoxidation process using Al can be transformed into other forms of oxide inclusions by a well-known process called calcium treatment, as reported by various researchers such as Abdelaziz, Megahed, El-Mahallawi and Ahmed (2009), Chen et al. (2015), Lis (2009), and Pires and Garcia (2004). The modification of an  $\text{Al}_2\text{O}_3$  inclusion through calcium treatment is done by adding alloying elements such as Calcium during secondary steelmaking. Lis (2009) suggests that an  $\text{Al}_2\text{O}_3$  inclusion in molten steel can be modified successfully with a CaO range of between 25% to 60%. The calcium treatment process is usually used in aluminium-killed (Al-killed) steels during secondary steelmaking to transform the solid  $\text{Al}_2\text{O}_3$  inclusion into calcium aluminate ( $\text{CaO}-\text{Al}_2\text{O}_3$ ) phase inclusions that have low liquidus temperatures compared to the steel melt (Pires & Garcia, 2004; Abdelaziz, et al., 2009; Lis, 2009; Chen et al., 2015).

Studies conducted by Abdelaziz et al. (2009) and Verma et al. (2012) show that modified calcium aluminate inclusions are globular-shaped, have a smaller cluster size and are less abrasive compared with solid  $\text{Al}_2\text{O}_3$  or MA inclusions that have dendritic morphology at rolling temperatures. The calcium treatment process also ensures that cleaner steel products with relatively low oxide contents are produced. Furthermore, from an operational control point of view, an effective calcium treatment process modifies solid  $\text{Al}_2\text{O}_3$  or  $\text{MgO}.\text{Al}_2\text{O}_3$  spinel inclusions, thus reducing potential submerged entry nozzle (SEN) clogging during steel casting (Abdelaziz et al., 2009). Ye, Jönsson and Lund (1996) indicate that the inclusion evolution sequence for Al-killed steel treated with calcium could follow a route such as  $\text{Al}_2\text{O}_3 \rightarrow \text{CA}_6 \rightarrow \text{CA}_2 \rightarrow \text{CA} \rightarrow (\text{C12A7}, \text{C3A})$ , where C12A7 and C3A

are considered lower melting phases at a steelmaking temperature. This pattern can depend on the elemental contents such as Ca, Al, O being present in the molten steel.

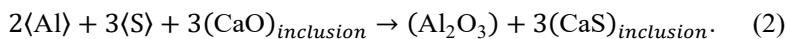
### **2.1.2 Inclusion formation and evolution process**

Extensive studies have been conducted concerning the formation, evolution and modification mechanisms on inclusion systems such as CaO–Al<sub>2</sub>O<sub>3</sub>, MgO–CaO–Al<sub>2</sub>O<sub>3</sub> and MgO–CaO–Al<sub>2</sub>O<sub>3</sub>–CaS (Seo, Kim, Jo, Suk & Byun, 2010; Yang, Li, Wang, Li & Lin, 2011; Verma et al., 2012; Ono, Mikib, & Hasegawac, 2014; Zhao, Li, Bao & Yang, 2015; Gollapalli et al., 2018; Tabatabaei, Coley, Irons & Sun, 2018). The implementation of these findings concerning non-metallic inclusions can potentially be useful to steelmaking industries to optimise the process and work towards achieving improved and high-quality steel products. Poirier (2015), and Yan et al. (2015), Park and Park (2016), Deng, Zhu and Sichen (2016), Miao, Haas, Sharma, Mu and Dogan (2018) have shown that interaction between molten steel and slag or the refractory can also influence an inclusion’s chemical compositions, morphologies, physicochemical properties and volume fractions in the steel melt or final steel product.

Additionally, the presence of elements such as S, Mn, or Mg within the steel melt can influence the formation and modification mechanism for inclusions. During the calcium treatment process for Al-killed steels, the calcium addition needs to be in the correct range for successful modification into calcium aluminates. For example, excess Ca and the high content of elements such as sulphur (S) in the molten steel, or a drop in activity of Al<sub>2</sub>O<sub>3</sub> below a critical level can lead to the formation of a CaS inclusion according to Pires and Garcia (2004). Holappa and Helle (1995) and Jing, Shu-Sen, and Zi-Jian (2013) have simplified the reaction for the formation of CaS, which can be expressed as



and



As well as this, adding too small an amount of Ca potentially results in the incomplete evolution of the solid Al<sub>2</sub>O<sub>3</sub> inclusions, therefore transforming them into solid calcium-aluminate (CaO–Al<sub>2</sub>O<sub>3</sub>) phases such as CA<sub>2</sub>, CA<sub>6</sub> (Sun, Waterfall, Strobl, Liao, Holdridge, 2017) and can cause clogging in casting. Jing et

al. (2013) have demonstrated that the route of modification and calcium content in the molten steel can affect the final inclusion composition.

The evolution and formation of inclusions associated with Al-killed calcium-treated steels can potentially take the following routes:

- *Alumina ( $Al_2O_3$ )* → *calcium-aluminates such as CA2, CA, C12A7 and C3A*: This is a situation where the deoxidation process using Al, and calcium treatment process are relatively considered auspicious. This route generally contains full liquid inclusion of C12A7 or partial liquid inclusion mixtures of C12A7-CA or C12A7-C3A at the casting temperature as discussed in studies conducted by Choudhary and Ghosh (2008), and Jing et al., (2013).
- *Alumina ( $Al_2O_3$ )* → *spinel (MA)* → *multi-component of CaO-MgO- $Al_2O_3$* : The potential formation of a MgO. $Al_2O_3$  spinel inclusion with other calcium-aluminates phases in a CaO-MgO- $Al_2O_3$  ternary system can be generated during the deoxidation stages through to the Ca treatment in the molten steel (Seo et al., 2010; Yang et al., 2011; Verma et al., 2012; Jiang et al., 2013; Ono et al., 2014; Tabatabaei et al., 2018).
- *Alumina ( $Al_2O_3$ )* → *calcium-aluminates ( $CaO-Al_2O_3$ )* → *multi-component of calcium aluminates and sulphides (such as CaS)* → *[CaO- $Al_2O_3$ ]-CaS*: The formation of a multiphase system of CaO- $Al_2O_3$ -CaS for Al-killed steel treated with calcium is generally associated with having excess Ca during the Calcium treatment process in the presence of higher S content in the steel melt (Nadif, Lehmann, Burty and Domgin, 2007 and Gollapalli et al., 2018).

### **2.1.3 Classification of inclusions**

A non-metallic inclusion can be considered indigenous (endogenous) or exogenous based on its sources (Kiessling, 1978; Way, 2001; Zhang & Thomas, 2006; Sahai & Emi, 2007). The types of inclusions originate from the interaction that occurs between active or dissolved oxygen, deoxidants such as aluminium (Al), and the molten steel during the steelmaking process. Indigenous inclusions are formed within the liquid steel. Indigenous inclusions can further be subdivided into primary and secondary endogenous inclusions. Primary endogenous inclusions are generated at liquid steelmaking temperatures; an example is deoxidation products such as solid  $Al_2O_3$  (Zhang & Thomas, 2006; Sahai & Emi, 2007). Secondary endogenous inclusions are attributable to the formation of inclusions during cooling and the solidification of steel melt (Zhang and Thomas, 2006), while exogenous

inclusions are formed mainly as a result of entrapped slag or refractory interactions with molten steel (Zhang and Thomas 2006).

Based on Papers I–V included for this study, the routes suggested by Jing et al. (2013) and the classification carried out by Thunman and Sichen (2008), non-metallic inclusions for Al-killed Ca treated steels can be grouped as follows:

#### *Group 1 - CaO–Al<sub>2</sub>O<sub>3</sub>*

This group of inclusions is formed within the CaO–Al<sub>2</sub>O<sub>3</sub> binary system. Three different phases of calcium aluminate inclusions are analysed in this study. These are low liquidus temperature phases of 12CaO·7Al<sub>2</sub>O<sub>3</sub> (C12A7), monocalcium aluminate, CaO·Al<sub>2</sub>O<sub>3</sub> (CA) and tricalcium aluminate, 3CaO·Al<sub>2</sub>O<sub>3</sub> (C3A).

#### *Group 2 - [CaO–Al<sub>2</sub>O<sub>3</sub>] + MA spinel*

This group presents a situation where CaO–Al<sub>2</sub>O<sub>3</sub> inclusions [12CaO·7Al<sub>2</sub>O<sub>3</sub> (C12A7), CaO·Al<sub>2</sub>O<sub>3</sub> (CA) or 3CaO·Al<sub>2</sub>O<sub>3</sub> (C3A)] can envelop around magnesium–aluminate spinel (MA). Therefore, the presence of MA spinel surrounded by CaO–Al<sub>2</sub>O<sub>3</sub> can be used to distinguish group 2 from group 1.

#### *Group 3 - (CaO–Al<sub>2</sub>O<sub>3</sub>) + CaS*

This inclusion group is based on a CaS shell enveloping around the CaO–Al<sub>2</sub>O<sub>3</sub> inclusions such as C12A7, C3A or CA (as in group 1). The existence of this group can be linked to introducing an excess calcium-containing element during the Ca treatment in the presence of higher S content in the steel melt.

#### *Group 4 - CaO–Al<sub>2</sub>O<sub>3</sub> + spinel + CaS*

Inclusions for this group are derived from the group 3 inclusion with the additions of MA spinel to illustrate a situation where multi-component inclusions consisting of sulphides (CaS), Ca-aluminates and MA spinel can be formed. This can occur when the casting and inclusion modification processes are less effective relative to suppressing a potentially harmful element.

The ideal sequence discussed and suggested by the researchers demonstrates that for Al-killed steel treated with calcium, the general goal is to generate a low melting calcium aluminate inclusion such as those in group 1. However, the

modification and formation mechanism can generate relatively detrimental multiphase inclusions during ladle operations or surface quality challenges that may fall out of expectations and can be associated with groups 2, 3 or 4. These multiphase inclusions can be traceable starting from the deoxidation process through to a Ca treatment for Al-killed steel with appreciable contents of Mg and S in the molten steel. Consequently, there is a need to embrace suitable characterisation techniques that assist in studying a relatively more uncomplicated inclusion system to a potentially complex inclusion system such as  $\text{Al}_2\text{O}_3 \rightarrow \text{MgO} \cdot \text{Al}_2\text{O}_3$ , (MA)  $\rightarrow \text{CaO} \cdot \text{Al}_2\text{O}_3$  (CA)  $\rightarrow \text{MgO} \cdot \text{Al}_2\text{O}_3 - \text{CaS} - (\text{CaO} - \text{Al}_2\text{O}_3)$

## 2.2 Characterisation and assessment techniques

The need for continuous improvement for steel cleanliness has encouraged the development of numerous analytical techniques for the characterisation of non-metallic inclusions found in the steel matrix. Depending on the type or purpose of assessment, non-metallic inclusion characterisation techniques can be classified differently. Literature from Zhang and Thomas (2003) has provided a detailed list of analytical techniques classified as direct or indirect methods. The methods stated by Zhang and Thomas (2003) have all contributed and continue to play a significant role as metallurgical approaches for the study of inclusions in steel samples.

However, the selection of suitable characterisation techniques for the identification and analysis of inclusions depends on the duration required for sample preparation, inclusion size, level of accuracy, and reliability of methods. Therefore, to meet steelmakers' expectations, it will be more appropriate, if possible, to have an analytical technique (or techniques) that are relatively fast, involve less sample preparation, and produce accurate or reliable analysis results. This will play a vital role in estimating and will potentially be used to control inclusions in the molten steel before or during the casting process. Numerous applications of vibrational spectroscopy such as Raman spectroscopy have proved to be a versatile and robust instrument to present some of the features listed in this section.

## 2.3 Brief background of Raman spectroscopy

As an analytical technique, Raman spectroscopy is a type of vibrational spectroscopy that operates by using an inelastic light scattering effect for the excitation of vibrational modes of molecules in a material which can either be solid,

liquid or even gas ( Harris & Bertolucci, 1978; Nakamoto & Brown, 2003). The Raman effect predicted and briefly explained as the change in wavelength when light is passed through a material or a set of molecules in harmonic vibrations (Nakamoto & Brown, 2003), was experimentally demonstrated by Chandrasekhra Venkata Raman in 1928 (Raman & Krishnan, 1928) and named after him. This new optical scattering phenomenon discovery won the Nobel Prize in Physics in 1930 in recognition of C.V. Raman's contribution to spectroscopic studies. The use of Raman spectroscopic studies for materials was minimal because the Raman signals were very weak. However, technological advances in Raman spectroscopic instrumentation resulted in the use of lasers that give high irradiation when the laser beam is focused on the material, therefore improving the Raman signals (Das & Agrawal, 2011; Lipiäinen et al., 2018).

According to Smith and Dent (2005), the general principle of Raman spectroscopic measurement also illustrates that Raman spectroscopy operates on the use of a laser source (monochromatic light) to generate intense electromagnetic radiation, and when focused on a material, it interacts with its components. This results in the scattering of the radiation in different wavelengths that create a characteristic spectral fingerprint of atomic vibrations. Generally, the change in vibrational frequency can be related to features such as the molecular group, the nature of bonds, and the chemical nature of the atoms that are found in the sample (Nakamoto & Brown, 2003).

When the monochromatic light from the laser interacts with the molecules in the material, the incident photons or radiation are scattered as Raman scattering or Rayleigh scattering according to Smith and Dent (2005), and Nakamoto and Brown, (2003). Raman scattering is an inelastic scattering that occurs when the scattered photons have to change energy from the incident, or due to the absorption or excitation of a vibrational mode of the molecule in a material (Nakamoto & Brown, 2003; Smith & Dent, 2005). The shift in energy attributable to the scattered photons for Raman scattering is referred to as the Raman shift. Rayleigh scattering takes place when there is no energy change between a scattered photon and the incident photons and with the scattering considered elastic (Nakamoto & Brown, 2003; Smith & Dent, 2005).

Based on the excited states associated with the vibrational modes of the molecule in a sample (Smith & Dent, 2005), two types of Raman scattering can be established:

- *Stokes scattering* – Is a result of a molecule at the ground vibrational state which can absorb the energy from the incident photon and move to an excited or higher vibrational state. The loss of photon (energy loss) resulting from the difference between the ground state and the excited state is referred to as Stokes scattering.
- *Anti-Stokes scattering* – Is a situation where a molecule already in an excited state absorbs the photon and returns to a ground state. The incident photon energy gained from the difference between the ground vibrational state and the excited state is defined as anti-Stokes scattering.

Figure 2 is the Jablonski diagram that illustrates the interaction of incident photons with the molecules in a sample can be related to using energy-transfer mechanisms, as explained by Colthup, Daly and Wiberley (1990). Rayleigh (elastic scattering) occurs as a result of the transition starting within the same vibrational energy level and therefore there is no frequency change  $\nu_0$  or loss of energy. For Raman scattering or inelastic scattering, waves with frequencies of  $\nu_0 + \nu_i$  occur when scattered photons are increased in the frequency by  $\nu_i$  and are considered anti-Stokes Raman scattering (Das & Agrawal, 2011). In addition, Stokes Raman scattering relates to a situation when there is a decrease in frequency  $\nu_0 - \nu_i$  attributed to the scattered photon. According to Smith and Dent (2005), Raman scattering intensity can be expressed as

$$I = KI_0 a^2 * (\nu_0 \pm \nu_i)^4, \quad (3)$$

where  $K$  denotes a series of constants,  $a$  is polarizability constant and  $I_0$  represents the intensity of the incident radiation.

Additionally, Boltzmann's equation shows that the relationship and ratio between the Stokes Raman and anti-Stokes Raman scattered photons can be associated with a vibrational ground and an excited states population and is expressed as (McCreery, 2001)

$$\frac{I_{Stokes}}{I_{anti-Stokes}} = \left( \frac{\nu_0 - \nu_i}{\nu_0 + \nu_i} \right)^4 e^{\frac{h\nu_i}{K_B T}}, \quad (4)$$

where,  $K_B$  represents the Boltzmann constant,  $h$  is Planck's constant and  $T$  is the absolute temperature.

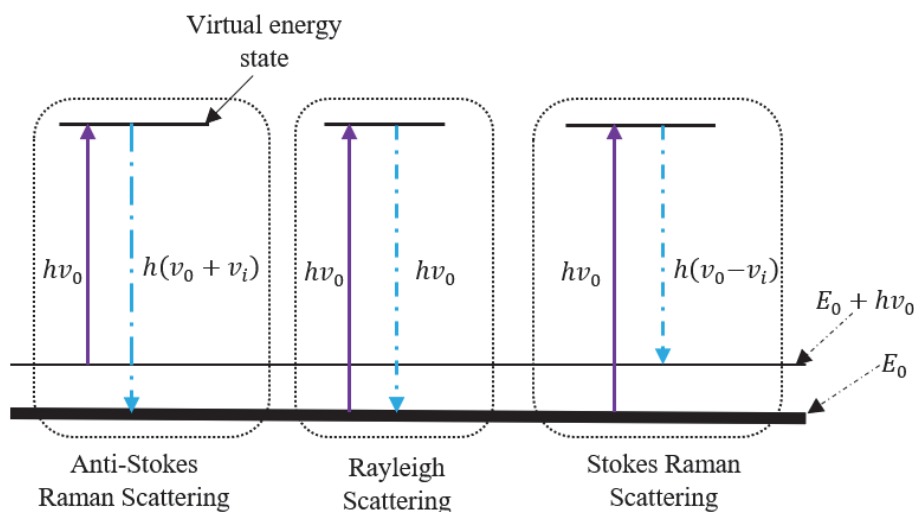


**Fig. 2. Energy level diagram showing Rayleigh (elastic) and Raman or inelastic scattering.  $\nu_0$  is the frequency of the radiation source, and  $\nu_i$  is the molecular vibration for the sample analysed (Redrawn from Smith and Dent, 2005).**

Stokes scattering is more preferred and is used for Raman spectroscopic measurements compared to anti-Stokes scattering at room temperature. This is because at an ambient temperature, most of the molecules in a material exist in the ground state. Therefore, as a result of an incident photon, Raman scattering is dominated by Stokes Raman scattering (Smith & Dent, 2005). Stokes scattering generally has more molecules in the ground vibrational state relative to the molecules found in excited states of a material (Smith & Dent, 2005). However, the potential challenge associated with Raman scattering is that a small fraction of the scattered photons is Raman scattered (Smith & Dent, 2005).

According to Chase (1994), this can be mitigated with the use of highly efficient laser sources to excite the molecule in the material measured, and the Rayleigh scattering can be suppressed by using a filter. The Raman spectrum acquired from a sample is a graphical representation of the measurement results from the sample, with the intensity of the scattered light plotted on the  $y$ -axis against the frequency of light on the  $x$ -axis as shown in Figure 3. The Raman shift is equivalent to the energy from the vibrational states of the molecule. The frequency plot on the  $x$ -axis is measured with a unit referred to as a wavenumber and is denoted as reciprocal centimetres ( $\text{cm}^{-1}$ ). For a sample measured with Raman spectroscopy, Figure 3 further illustrates a schematic diagram labelled as (i – iii)

that shows the relevant information that can be acquired from a Raman spectrum which includes:

- i. The intensity ( $I$ ) shows the specific component concentration in the sample measured.
- ii. Raman band (shift) position is used to illustrate the measured sample phase, structure or stoichiometric content.
- iii. The full width at half maximum (FWHM) shows the crystallinity, the defects or doping of the sample measured and the Raman band (shift) direction could be attributable to the effect of stress, pressure, or temperature.

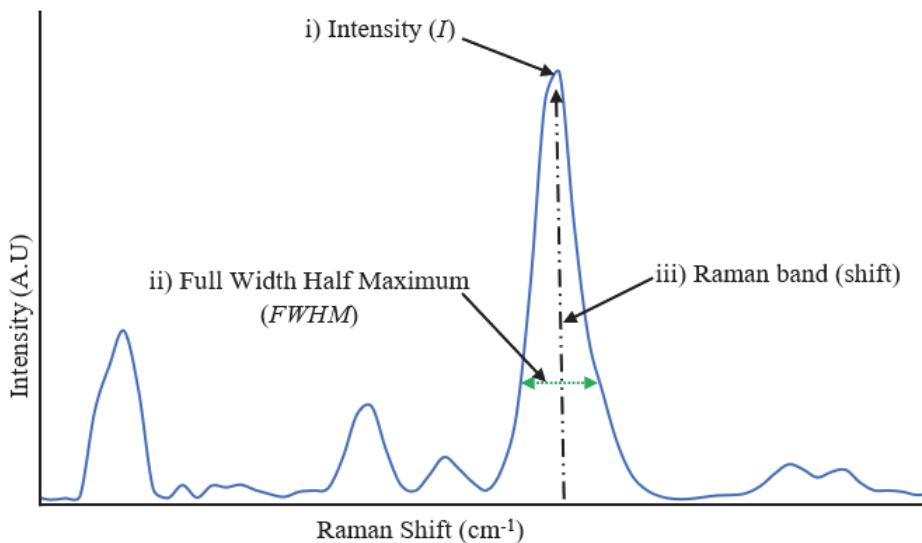


**Fig. 3. A schematic diagram of a Raman spectrum and corresponding measurement data information.**

### **2.3.1 Applications of Raman spectroscopy**

From literature, Raman spectroscopy has shown its vital role to research developments and applications as an analytical technique. The use of Raman spectroscopy had been reported in fields of research such as in pharmaceuticals (Vankeirsbilck et al., 2002) and material science (Tian et al., 2006). Additionally, as a characterisation technique, Raman spectroscopy has been used to study some

inclusions (Hirlimann, Jouanne, & Forriès, 1992; Cooper, Elliott & Young, 2003; Li & Hihara, 2017) and metallurgical slag structural analysis (Park, 2013). Below are some advantages associated with the use of Raman spectroscopy for materials analysis:

- It is generally considered a relatively non-destructive characterisation technique; however, for heat-sensitive samples, the laser irradiation can potentially react with the sample. The use of relatively low laser power can be used to minimise the destructive effect on the sample.
- There is relatively less duration or an easy sample preparation process, and a Raman spectrum can be obtained from material non-invasively.
- The instrument is quite easy to operate, and usually each measurement can be carried out in just a few seconds or minutes.
- Additionally, Raman spectroscopy is considered a promising tool for the study of materials since specific components in a material can be identified based on the Raman spectrum that serves as a characteristic fingerprint or signature of the components measured in the material. As well as this, it can be used for both qualitative and quantitative analysis (Dandeu et al., 2006; Muñoz Tabares & Anglada, 2010).

### **2.3.2 Limitations of Raman spectroscopy**

The use of any analytical instrument will generally have some demerits; similarly, Raman spectroscopy has some limitations that should be considered when conducting sample measurement. Some examples of the limitations associated with Raman spectroscopy include:

- *Fluorescence effect*: A potential challenge with the use of Raman spectroscopy to conduct measurements depends on the level of fluorescence interference with the Raman bands (Vankeirsbilck et al., 2002). Studies conducted by Lipiäinen et al. (2018) have demonstrated that a recent technological development can be used to suppress the fluorescence interference by ensuring that the Raman signals are obtained quickly relative to the fluorescence effect by using time-gated techniques.
- *Excitation intensities effect*: Very high excitation intensities (laser power) can thermally decompose the sample, especially heat-sensitive materials.

### 2.3.3 Raman spectroscopy instrumentation

The main components for a Raman spectroscopy typically include an excitation source, a rejection filter, a diffraction grating, a detector and a source of recording the Raman spectrum, as illustrated with a schematic diagram in Figure 4. The excitation source consists of a laser source; the selection of a laser source may depend on the spot size required and wavelength. The laser source illuminates the samples via fibre optic cables or lens, and the Raman scattered light is collected with optical fibre. The scattered light is filtered using a rejection filter that is used to block the Rayleigh source from the sample excited with the laser source (Chase, 1994). The detector is used to analyse the emitted Raman scattered light. Finally, a spectral analysis system is used to analyse the collected Raman spectra.

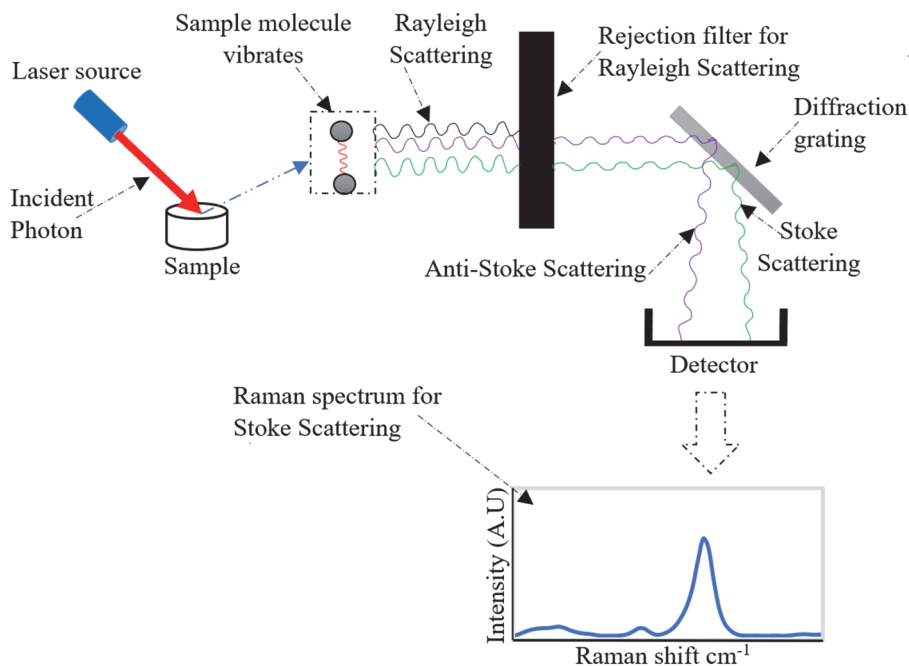


Fig. 4. Simplified schematic diagram of Raman spectrometer instrumentation.

## 2.4 Calibration model identification and multivariate analysis

According to Cooper (1999) and Harrell (2001), a calibration model and multivariate analysis are widely used for characterising materials measured with Raman spectroscopy. In using a calibration model, the relationship between different Raman bands (peaks) ratios and the sample weight percentage or phase content can be established and analysed. For analysing the phase content of the binary sample, the use of linear regression constructed between the relative Raman intensity of the peak ratios and the phase content in the sample can be carried out. However, as the individual components or phases in a sample increase (more than two components), potential overlapping of Raman peaks or variable collinearity in the Raman spectra data can cause the inaccurate estimation of the specific components in the samples. Consequently, detailed mathematical models are required to process and enhance the quantitative estimation for the individual constituents from the Raman spectra data treatment.

### 2.4.1 Model selection

The relationship between a specific component in a sample and the measured Raman data for binary samples can be established using a calibration model. The calibration model can further be used for estimating the variation in the component content in the samples by considering the relative intensities for the Raman peaks associated with the phases found in the Raman spectrum. According to Harrell (2001), the calibration model feature candidate can be expressed as

$$x_c = \frac{I_k}{(I_n + I_k)}, \quad (5)$$

where  $x_c$  is used to denote the model calibration feature candidate,  $I_n$  represents the intensity that relates to the Raman shift  $n$ , and  $I_k$  represents the intensity for the Raman shift at  $k$ .

Prior to the analysis, the raw Raman spectra data obtained from the Raman spectroscopy measurement are subjected to normalisation. A linear regression calibration model can be constructed between normalised relative intensities of the Raman peaks obtained from the total summed Raman spectra and the phase contents in the sample. Harrell (2001) suggest that the error function associated with the calibration parameter can be expressed as

$$\min \sum_{i=1}^k (y_{i,t} - \hat{y}_{i,t})^2 = \min \sum_{i=1}^k \left( y_{i,t} - \left[ b_1 \frac{I_{k,t}}{(I_{n,t} + I_{k,t})} + b_0 \right] \right)^2. \quad (6)$$

In addition, with Moore-Penrose inversion, according to Harrell (2001), the least-squares solution of the error function can be expressed as

$$\hat{b} = (X^T X)^{-1} X^T y, \quad (7)$$

where the estimated parameter  $b_0$  is the intercept,  $b_1$  is the slope,  $\hat{b}$  denotes the least squares estimate,  $X$  is the data design matrix,  $t$  represents the training subset and  $y$  is the response vector or dependent variable.

Baumann (2003) as well as Baumann and Stiefl (2004), have shown that a leave-multiple-out cross-validation procedure can be used to evaluate the model performance for each of the calibration variables for a calibration model. Additionally, the use of a leave-multiple-out cross-validation can be used to obtain a very stable model (Baumann & Stiefl, 2004). The data used for the analysis can also further be split to approximately 20% for validation and 80% used for training in the cross-validation process.

The assessment for the model distribution and performance of the calibration parameters can be done by carrying out for about the cross-validation  $4N$  times. The final calibration model selections are presented in equations 8 and 9, where  $k$  is the number of data points in the validation set,  $N$  is the number of data points in the training set, and with  $l$  as the split repetition.

The assessment for the model distribution and performance of the calibration parameters can be done by carrying out for about the cross-validation  $4N$  times. The final calibration model ( $C_{final}$ ) selection is presented by

$$C_{final} = \min \frac{1}{4N} \sum_{l=1}^{4N} MAE_{l,t} + MAE_{l,cv}, \quad (8)$$

where

$$MAE = \frac{1}{k} \sum_{i=1}^k |y_{i,t} - \hat{y}_{i,t}|, \quad (9)$$

$k$  is the number of data points in the validation set,  $N$  is the number of data points in the training set, and with  $l$  as the split repetition.

Baumann et al. (2004) demonstrate that the stability of the calibration model can be estimated by using the ratio of the mean and the standard deviation for a standardised regression coefficient, based on the split  $4N$  repetitions presented by equation

$$S_i = \frac{\frac{1}{4N} \sum_{j=1}^{4N} b_{i,j}}{\sqrt{\frac{1}{4N} \sum_{j=1}^{4N} (b_{i,j} - \bar{b}_{i,j})^2}}, \quad (10)$$

where  $b_{i,j}$  represents the identified regression coefficient for training subset  $j$  and variable  $i$ . The model parameter distribution that has reduced average mean absolute error is considered to have the most suitable value for the Raman spectra data treatment based on the relative intensities peaks ratios and the phase fraction in the sample. Consequently, the final performance of the model can be evaluated using a coefficient of determination ( $R^2$ ) and mean absolute error (MAE).

#### **2.4.2 Multivariate analysis**

The use of robust multivariate techniques, such as successive projection algorithm (SPA), standard normal variate (SNV), and partial least squares (PLS) regression (Geladi & Kowalski 1986; Barnes, Dhanoa & Lister 1989), are some of the standard tools for extracting and conducting a quantitative analysis of Raman spectra data obtained from multi-components samples measured using Raman spectroscopy. For Raman spectra data, the use of partial least square (PLS) regression presents the opportunity to extract and analyse multi-component samples where there is a potential peak overlap (Heinz, Savolainen, Rades & Strachan, 2007). Multiple linear regression (MLR) used to treat Raman spectra data has shown to be potentially very unstable or provide inaccurate results in estimating the individual components in samples (Wold, Ruhe, Wold & Dunn III, 1984; Grinberg & Rodriguez, 2019). Therefore, the use of PLS regression provides relatively better options for multi-component Raman spectra data analysis.

In analysing multi-component samples measured with Raman spectroscopy, the spectra data is usually split into training and testing (external validation) sets. Depending on the nature of the Raman spectra data obtained, the process can require the use of normalisation to be carried out on Raman spectral datasets, as explained by Beattie, Glenn, Boulton, Stitt and McGarvey (2008). Generally, the testing (external validation) set is used for the assessment of the model performance.

Raman spectra of a sample containing multiple phases can contain numerous Raman peaks. Therefore, there is a requirement to use a pre-processing process to reduce the Raman spectral data dimensionality for a relatively very stable calibration model for the subsequent operation such as PLS (Wold et al., 1984; Fernandes de Oliveira Penido, Pacheco, Lednev & Silveira, 2016). Additionally, Guyon and Elisseeff (2003) have shown that feature selection can be used to improve upon the estimation performance by extracting the relevant information from the Raman data to predict the phase composition in the sample and to enhance the interpretability.

A standard normal variate (SNV) pre-processing algorithm is used to correct any potential background effect or baseline shifting (Barnes et al., 1989). Guyon and Elisseeff (2003) have also demonstrated that the use of SNV transformation and centring improves Raman spectra data analysis. Additionally, the SNV can be used to reduce potential sources of non-linearity that may be associated with the concentrations of the analysis from the measured Raman spectra obtained (Guyon & Elisseeff, 2003). In addition, the potential challenges of the feature selection can be reduced by applying deterministic search engines such as successive projection algorithm (SPA) as suggested by Araújo et al. (2001). SPA provides the opportunity to select the relevant features and minimises the collinearity within the chosen feature set.

Baumann (2003) has suggested that the multivariate technique, such as PLS regression model's performance, improves when the feature selection is carefully carried out so that it reduces information from the Raman signal, from which a maximum estimate is obtained. According to Baumann (2003), an objective function addresses the potential challenges with the feature selection cross-validation set. The objective function can be expressed as (Baumann, 2003)

$$\min J(b, X) = \min \sum_{i=1}^k (y_{i,iv} - f(b, X_{i,iv}))^2, \quad (11)$$

where  $J$  represents the objective function,  $X$  is a matrix with  $k$  columns and  $n$  rows,  $b$  is the model parameter vector, and  $f$  is the functional relationship with the signal features.

A subsequent multivariate process, such as partial least squares (PLS) regression, is applied to the pre-processed Raman data. PLS regression presents a promising multivariate technique for Raman spectral data analysis, as shown in the literature available which demonstrates its applicability. For a typical Raman spectral data multivariate analysis using PLS regression, the data is usually randomly split into calibration and testing sets. The calibration set is used to generate the quantification model, and the testing set is for predicting the model.

In the PLS regression analysis, an average spectral covariance is established between the Raman spectra data and concentration of the different phases, where  $X$  variables serve as the spectra intensities, and  $Y$  variables represent the concentration for the components in the sample. In the calibration procedure, the Raman spectra measured from the samples the  $X$  variables represent the independent and  $Y$  is dependent the variable. According to de Almeida, Correa, Rocha, Scafi and Poppi, (2013),  $X$  matrix can be denoted with  $n$  as the number of samples analysed and  $w$

represented as the constituent number; the dependent variable  $Y$  is labelled so that  $z$  represents the number of properties of the components. The PLS regression expressed in the independent  $X$  and dependent  $Y$  variables can be given by equations (Poppi et al., 2013)

$$X = TP^T + E_X \quad (12)$$

and

$$Y = UQ' + E_Y, \quad (13)$$

where  $T$  denotes the score matrix for  $X$  variables,  $P^T$  represents the loading for the variables  $X$ , and  $E_X$  is the residue for  $X$ . Furthermore,  $U$  is the score matrix for  $Y$  variables,  $Q'$  is the loading for the variable  $Y$ , and  $E_Y$  is the residue for  $Y$ .

In assessing performance for the PLS regression calibration model, different statistical parameters such as the correlation coefficient  $R^2$ , the root mean standard error in (RMSE), the root mean square error of calibration (RMSEC) and the root mean square error of prediction (RMSEP) are used in the model evaluation. The assessment features to assist in determining how well the individual component in the samples can be quantified; RMSE according to Kachrimanis, Braun & Griesser (2007) and Lopes et al. (2018) is expressed as

$$\text{RMSE} = \sqrt{\frac{\sum_{i=1}^n (y_i - \hat{y}_i)^2}{n}}, \quad (14)$$

where  $y_i$  is the reference value,  $n$  indicates the number of samples, and  $\hat{y}$  represents the calculated value.

### *Model validation*

To further enhance prediction performance and effectiveness for the calibration model in quantifying the specific component concentration in a sample, additional statistical parameters such as the range error ratio (RER) and the ratio of prediction to deviation (RPD) can be estimated. According to Lopes et al. (2018), the ratio of prediction to deviation (RPD) and the range error ratio (RER) can be expressed as

$$\text{RDP}_{\text{pred}} = \frac{\text{SD}_{\text{PRD}}}{\text{RMSEP}} \quad (15)$$

and

$$\text{RER} = \frac{(\text{Max} - \text{Min})_{\text{refv}}}{\text{RMSEP}}, \quad (16)$$

where  $\text{SD}_{\text{PRD}}$  is the standard deviation for the prediction set,  $\text{RMSEP}$  is the root mean square error of prediction,  $\text{Max}$  is maximum and  $\text{Min}$  is minimum (subscript *refv* denotes reference values).

The suggested criteria (Saeys, Mouazen, & Ramon, 2005; Quentin, Rodemann, Doutreleau, Moreau & Davies, 2017; Lopes et al., 2018) shows that if the RPD value is less than 1.5 ( $< 1.5$ ) and the RER is less than 4 ( $< 4$ ), the calibration model is considered unsatisfactory, while for a generally satisfactory model the RPD should range between 3–4.9 and the RER should be  $\geq 10$ . The excellent calibration model is said to be achieved when the RRD value is above 5 ( $> 5$ ) and  $\geq 15$  for the RER.

## 3 Experiment

### 3.1 Description of the experimental procedure

The raw materials used for this study were obtained from commercial suppliers with very high quality. Table 1 summaries the chemicals or phases obtained from a chemical supplier (Alfa Aesar) and those prepared in the laboratory of the University of Oulu process metallurgy research unit, Finland.

**Table 1. List of reagents or chemicals used for this study.**

Chemical	Purity (wt%)	Source
Aluminium oxide ( $\text{Al}_2\text{O}_3$ )	99	Alfa Aesar
Calcium oxide (CaO)	99	Alfa Aesar
Monocalcium aluminate $\text{CaO}\cdot\text{Al}_2\text{O}_3$	99	Alfa Aesar
Calcium sulphide (CaS)	99	Alfa Aesar
Magnesium aluminate spinel, $\text{MgO}\cdot\text{Al}_2\text{O}_3$	99	Alfa Aesar
Tricalcium aluminate, $3\text{CaO}\cdot\text{Al}_2\text{O}_3$	98–99	Prepared
$12\text{CaO}\cdot 7\text{Al}_2\text{O}_3$	98–99	Prepared

#### 3.1.1 Preparation of synthetic inclusion samples

Sintering process for  $12\text{CaO}\cdot 7\text{Al}_2\text{O}_3$  and  $3\text{CaO}\cdot\text{Al}_2\text{O}_3$ : Calcium aluminate phases of  $12\text{CaO}\cdot 7\text{Al}_2\text{O}_3$  (C12A7) and  $3\text{CaO}\cdot\text{Al}_2\text{O}_3$  (C3A) were prepared from calcium oxide (CaO) and aluminium oxide ( $\text{Al}_2\text{O}_3$ ) powders. The powders were weighed with an analytical weighing balance and thoroughly mixed with a ball mill. The mixture was sintered in a graphite crucible and placed in an aluminium crucible filled with graphite powder with varying grain sizes, as illustrated in Figure 5, showing the isometric view of the crucible setup. The sample sintering was carried out in a chamber furnace at a temperature of 1350 °C and programmed as shown in Figure 6. The sintering process was repeated three to four times with intermediate milling until the required phase was within a range of 98–99 wt%.

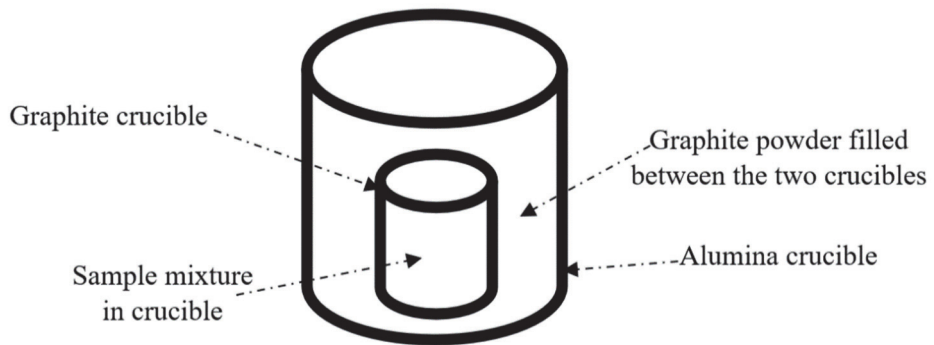


**Fig. 5.** The crucibles setup used for preparing the synthetic inclusion phases.

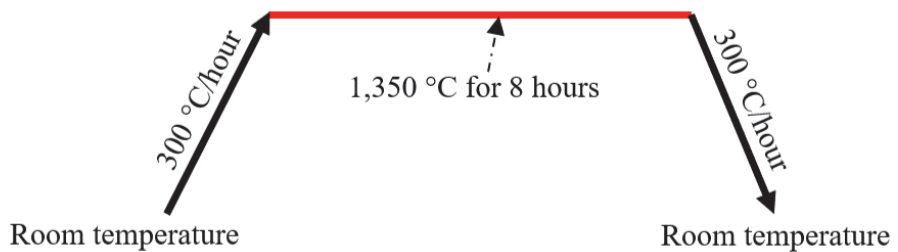


**Fig. 6.** A graphical trend showing the temperature program for preparing the synthetic inclusion phases of C12A7 and C3A.

### **3.1.2 Sample matrix**

A sample matrix for Papers I, II and III used for this study was prepared by measuring a varying weight percentage (wt%) of the starting phases (C12A7, CA, C3A, Al<sub>2</sub>O<sub>3</sub> and MgO.Al<sub>2</sub>O<sub>3</sub>) to generate the synthetic binary or ternary systems. The mixtures were thoroughly mixed, pressed into pellets, placed in a crucible, and sintering was performed in a chamber furnace at a temperature of 400 °C. The sintering was carried out at 400 °C to remove potential moisture in the sample in order to prevent or reduce the moisture content for subsequent analysis. For studies (Papers IV and V), which contained CaS, the synthetic binary and ternary inclusion systems were prepared by measuring the approximate proportions of MgO.Al<sub>2</sub>O<sub>3</sub>, CA, C12A7, C3A or CaS. Careful mixing was employed to achieve homogeneously prepared samples. CaS is quite sensitive to heat (as stated by the supplier, Alfa

Aesar) and this was also noted during initial experimental stages during the Raman spectroscopy measurements; therefore, subsequently, it was not suitable to heat the samples prepared as they were required to contain CaS as a component. Table 2 presents the specific phases used for studies in Papers I–V.

**Table 2. Synthetic sample mixtures for Papers I–V.**

Paper	Prepared phases
I	C12A7–CA and C12A7–C3A
II	Al <sub>2</sub> O <sub>3</sub> –MA, CA–MA, C12A7–MA and C3A–MA
IV	C12A7–CaS, C3A–CaS, CaS–MA, CA–CaS and Al <sub>2</sub> O <sub>3</sub> –CaS
III	C12A7–C3A–MA and C12A7–CA–MA
V	C12A7–CA–CaS, C3A–MA–CaS, MA–C12A7–CaS, C12A7–C3A–CaS and CA–MA–CaS

The weight percentage (phase fraction) matrix design for the binary samples for Papers I, II and IV, were ranged between 20–90 wt% for the two-component content. A simple relation, such as  $y\alpha + (100 - y)\beta \rightarrow 100$  (wt%), where  $\alpha$  and  $\beta$  are the phases present in the sample, is used to describe how the binary system was prepared for this study. For Papers III and V, the complete sample design matrix was used by considering  $k^n$  compositions, where  $k$  shows the number of design levels, and  $n$  denotes the design variables. Figure 7 illustrates examples of sample matrix presented in a ternary system for Paper III, which had a total of 43 samples for MA–C12A7–C3A (Figure 7 (a)) and 48 samples for C12A7–CA–MA (Figure 7 (b)).

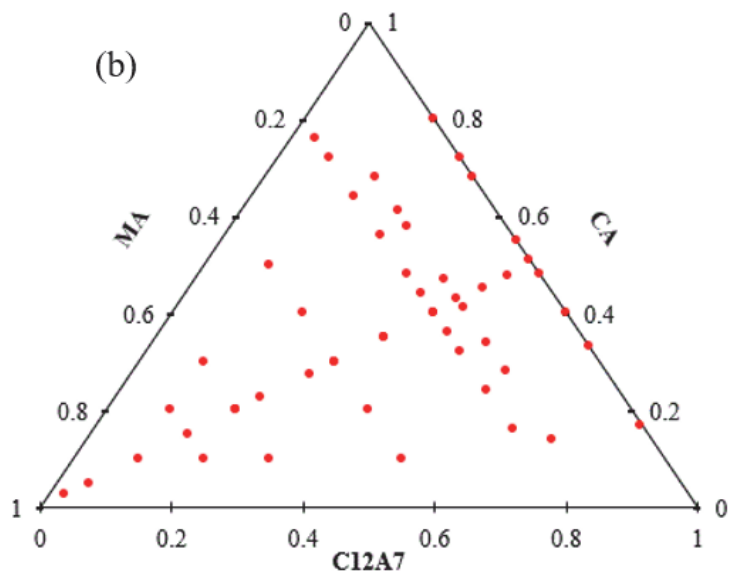
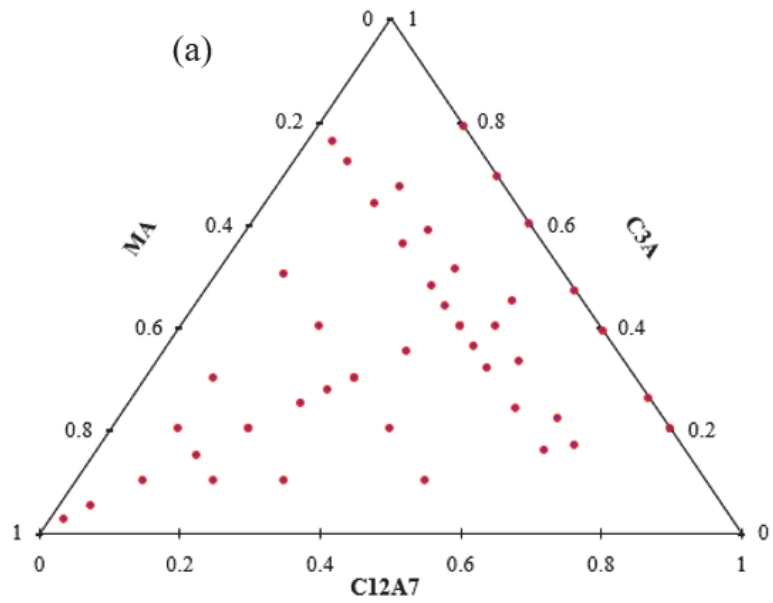


Fig. 7. Sample matrix for (a) C3A-C12A7-MA and (b) CA-C12A7-MA (Under CC BY license from Paper III © 2020 Authors).

## 3.2 Verification of synthetic inclusion samples prepared

The synthetic phases prepared in the laboratory (C12A7 and C3A) and those (CA, CaS and MgO·Al<sub>2</sub>O<sub>3</sub>) obtained from the supplier (Alfa Aesar) were assessed using both X-ray diffraction (XRD) and X-ray fluorescence (XRF). The phase fraction or weight percentage proportion used for preparing the samples matrix was further analysed with XRD and XRF to ensure that the homogeneous samples were achieved for subsequent measurements.

### 3.2.1 XRD and XRF

The phase identification for synthetic inclusion samples prepared for this study was carried out by using X-ray diffraction (XRD) instrument to estimate the specific component (weight percentage, wt%) in the samples. The XRD instrument utilised for this study was a Rigaku SmartLab with 9 kW rotating Cu anode (45 kV and 200 mA). Measurement was performed in Bragg-Brentano para-focusing geometry by using acquisition of 3 degrees per minute and 0.02 degrees per step. The instrument is also equipped with a 10 mm limiting slit found at the source side of the samples placed in standard glass holders, with 5-degree Soller slits used on both sides. A PDXL2 software suite with integrated access to a PDF-4 2018 database was used for estimating the weight percentage for the phases present in the samples measured with XRD. The elemental analysis was conducted using SuperQ software.

X-ray fluorescence (XRF) was used to estimate and verify the elemental composition of the samples. The samples' elemental analysis was performed using an XRF instrument provided by the University of Oulu's Centre for Material Analysis. A Panalytical Axios Max XRF model instrument that has an X-ray generator and Rh tube with a maximum power of 4 kW was used.

Further analyses were carried out to verify the homogeneity of the binary and ternary samples by measuring replicates of the prepared sample with the use of XRF and XRD. Consequently, some assumptions were taken into consideration to enable a comparison between the samples analysed with both XRD (phase identification) and XRF (elemental composition). These include:

- Estimating the weight percentage or phase fraction for C12A7, CA and C3A based on the elemental composition (CaO, and Al<sub>2</sub>O<sub>3</sub>) obtained from XRF analysis results, which was done by using the molar mass of 12CaO·7Al<sub>2</sub>O<sub>3</sub> for C12A7, CaO·Al<sub>2</sub>O<sub>3</sub> for CA and 3CaO·Al<sub>2</sub>O<sub>3</sub> for C3A.

- The samples analysed with the XRD instrument were considered to have stoichiometric phases, and therefore, the prepared samples were assumed to contain only the phase analysed by the XRD instrument.
- The XRD analysed data from the samples were normalised in the evaluation, from weight percentage (phase fractions) to elemental compositions, therefore making it possible to make a comparison with the XRF analysis results.
- Similarly, the XRF analysis data from the prepared samples were normalised to the weight percentage or as phase compositions for a relatively more straightforward compared to the XRD analysed sample phase composition.
- Additionally, all CaO estimated in the samples with the XRF analysis was assumed to be attributable to the calcium-aluminate ( $\text{CaO-Al}_2\text{O}_3$ ) phases present for the same samples identified with the XRD.
- All the Mg ( $\text{MgO}$ ) estimated in the sample mixture (which contained MA) based on the XRF elemental composition analysis was considered to be associated with the presence of the  $\text{MgO}\cdot\text{Al}_2\text{O}_3$  (MA) spinel phase in the sample, since the other components (phases) used for this study, do not have elemental Mg as its composition apart from MA.

### 3.3 Raman spectroscopic measurement

The Raman spectroscopy (TimeGated<sup>®</sup> 532 Raman spectrometer, TG532 M1) used for the study was supplied by TimeGate Instruments Ltd, Finland. The Time-gated Raman spectroscopy was used to acquire the Raman spectra from the samples. The main operating parameters obtained from TG532 M1 user's manual are illustrated in Table 3. There are a variety of excitation sources that can be used to irradiate the samples. The selection of the excitation sources (for the laser system) can be based on the spot size, resolution, wavelength and the sensitivity of the sample, and Table 3 shows some basic features of the laser used for this work. One of the phases (CaS) is very sensitive heat (high laser power); therefore, for studies (Papers IV and V) that had CaS as a constituent of the sample mixtures, extra care was taken to adjust the laser power accordingly to ensure that the Raman spectra measured from the samples were not significantly affected by any potential heat generated from the laser.

**Table 3. Basic features of time-gated Raman spectrometer Model TG532 M1.**

Instrument Component	Features
Laser	Centre wavelength; 532 nm, pulse repetition rate; 40–100 kHz, pulse width; <150 ps, average power; 30–60 mW and fibre-coupled.
Probe head	InPhotonics RPB532 with 105 $\mu\text{m}$ excitation and 200 $\mu\text{m}$ collection fibres.
Spectrometer	Fibre-coupled spectrograph with an optical resolution of approximately $13\text{ cm}^{-1}$ ; delay electronics; CMOS-SPAD array detector; auxiliary electronics, and mechanics.

Before the start of the Raman spectroscopy measurements, the samples (powders mixtures) were compacted into a cylindrical sample holder with a height of approximately 5.0 mm and a diameter of 20.0 mm. The laser beam was carefully focused on the sample. Figure 8 shows the time-gated Raman spectroscopy sample holder equipped with a rotating stage. The use of a rotating sample holder stage that ensures the illumination of the most section of the upper surface of the sample by a laser beam. All the Raman spectroscopy measurements were conducted at ambient conditions, at a spectra acquisition time of 1–3 minutes, with a wavenumber range between  $100\text{--}1,200\text{ cm}^{-1}$ , and a resolution of  $10\text{ cm}^{-1}$ . An average of three to five serial Raman measurements were conducted per sample. Generally, the Raman spectra /signal acquired within each sample in this work had insignificant variability in the Raman data and therefore, was considered relatively stable for the purpose of this study.

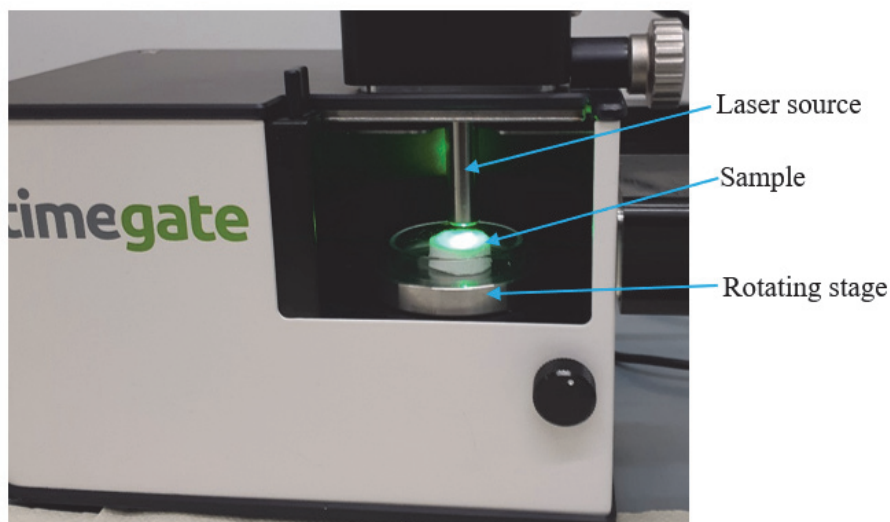


**Fig. 8. Time-gated Raman spectroscopy sample holder equipped with a rotating stage.**

The Raman spectral processing software was provided by The TimeGate Instruments Raman company (TimeGated Model: TG532 M1) for data acquisition and for pre-processing the series measurement data. The software offers one the possibility to view the measured raw data in various graphical types, and also to estimate the shot-noise-limited SNR as well as to distinguish between the luminescence and Raman through baseline fitting. The raw data could be collected in ASCII formats for subsequent treatment processing.

## 4 Results and discussion

This chapter summarises the main results concerning the application of Time-gated Raman spectroscopy from Papers I–V enclosed in this study into four sections. The first two sections present results from the sample's composition estimation (using XRD and XRF) and the Raman bands (shift) details for the synthetic phases used for this study. The third section presents the findings based on how to identify and quantify each synthetic inclusion phase content in the samples using Raman spectroscopy combined with calibration and multivariate models. Finally, the practical prospects are briefly discussed in the last section of this chapter according to the formation and modification mechanism routes (A, B and C) illustrated in Figure 9. The Paper I is assigned to route A, while Papers II and III are linked to route B, and Papers IV and V are associated with route C in Figure 9.

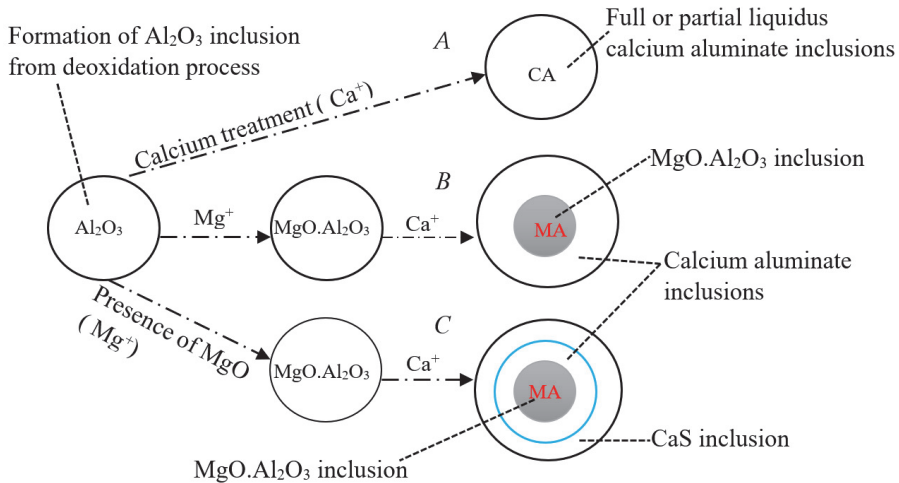


**Fig. 9. Schematic diagram illustrating possible routes for Al-killed calcium treated steel and how the results from Papers are presented.**

### 4.1 Identification of the sample's composition using XRF and XRD

The reference or starting constituents (phases) used in this study were prepared in the laboratory of process metallurgy research unit, University of Oulu (C12A7 and C3A) and others (CA, CaS and  $\text{MgO}\cdot\text{Al}_2\text{O}_3$ ) were acquired from a chemical

manufacturer. To estimate and verify the reference purity, XRD and XRF analyses were conducted to provide detailed information about the reference phases used to prepare the sample mixtures. Tables 4 and 5 are examples that are used to establish the relationship between XRD and XRF based on the results obtained from the analyses of the samples. These were carried out based on the estimated sample phase fraction or weight percentage (wt%) obtained using XRD, and the samples elemental analysis using XRF.

These two analytical techniques (XRD and XRF) provide relatively different analysis information for the sample measured. Table 4 presents a comparison between the XRF measured elemental composition values (CaO and Al<sub>2</sub>O<sub>3</sub>), and the XRD values calculated based on the weight percentages of CaO and Al<sub>2</sub>O<sub>3</sub>. In Table 5, the initial composition for the samples prepared (phase weight percentages evaluated using XRD) was compared with the XRF phases evaluated based on elemental analysis. It can be observed in Table 4 and Table 5 that there is a slight variation between the XRF and XRD results. For example, the XRD and XRF results for the C12A7-C3A binary phase samples presented in Table 5 have an average difference of 2.92 wt% and a standard deviation of 0.52 wt%.

It should be noted that the difference between the XRD and XRF analysed and calculated values did not significantly affect the measurements results in the subsequent process since these analytical methods also have their level of accuracy. Furthermore, the XRD and XRF analyses conducted on the samples serve as complementary techniques, and also the systematic difference does not have a significant impact since the analysis was made in relative terms. Some of the assumptions made during the estimation process to compare the two analytical techniques (XRD and XRF) are explained in section 3.2.1 of this thesis.

**Table 4. XRD and XRF analyses for binary calcium aluminates phases of C12A7-C3A (Reprinted with permission from Paper I © 2019 ISIJ).**

Sample	XRD analysis (wt%)		Calculated from		XRF analysis		Difference between	
	C12A7	C3A	XRD results (wt%) CaO	Al <sub>2</sub> O <sub>3</sub>	(wt%) CaO	Al <sub>2</sub> O <sub>3</sub>	XRD and XRF (wt%) CaO	Al <sub>2</sub> O <sub>3</sub>
X1	80	20	51.28	48.72	54.01	45.99	2.73	-2.73
X2	74	26	52.10	47.90	54.99	45.01	2.89	-2.89
X3	72	28	52.37	47.63	54.47	45.53	2.10	-2.10
X4	65	35	53.34	46.66	56.21	43.79	2.87	-2.87
X5	61	39	53.89	46.11	56.92	43.08	3.03	-3.03
X6	53	47	54.98	45.02	58.85	41.16	3.86	-3.86
X7	42	58	56.50	43.50	58.82	41.18	2.32	-2.32
X8	40	60	56.77	43.23	59.94	40.06	3.17	-3.17
X9	33	67	57.73	42.27	61.66	38.34	3.93	-3.93
X10	31	69	58.01	41.99	60.96	39.04	2.95	-2.95
X11	27	73	58.56	41.44	61.25	38.75	2.69	-2.69
X12	21	79	59.38	40.62	61.94	38.06	2.56	-2.56

**Table 5. Initial sample composition and XRF analyses for binary aluminate spinel-calcium aluminate phases of C12A7-MA and CA-MA (Reprinted [adapted] with permission from Paper II © 2020 ISIJ).**

Initial phase composition (wt%)			XRF results and calculated phase composition (wt%)				
C12A7-MA	C12A7	MA	Ca	Al	Mg	C12A7	MA
	85	15	32.4	26.4	2.9	85	15
	81	19	31.2	26.8	3.5	82	18
	76	24	29.8	27.8	3.4	81	19
	67	34	24.1	29.3	6.6	64	36
	43	57	17.5	32.5	8.5	50	50
	38	62	15.3	33.2	9.6	44	56
	29	72	9.6	35.2	12.1	28	72
	19	81	8.0	36.3	12.2	24	76
	10	91	4.5	37.8	13.4	13	87
5	95	2.4	39.0	13.8	7	93	
CA-MA	CA	MA	Ca	Al	Mg	CA	MA
	90	10	26.7	31.8	1.5	87	13
	80	20	23.6	33.4	2.3	79	21
	70	30	20.6	33.7	4.5	68	32
	60	40	18.2	34.5	5.6	55	45
	50	50	15.4	35.3	7.0	45	55
	40	60	13.0	36.9	7.3	37	63
	30	70	10.3	36.8	9.7	29	71
	20	80	7.6	37.8	10.8	21	79
	10	90	4.6	38.9	12.1	13	87
5	95	2.5	39.3	13.3	7	93	

## 4.2 Identifiable Raman bands for synthetic inclusion phases

Table 6 presents the Raman bands or shift ( $\text{cm}^{-1}$ ) for the synthesised inclusion phases of CA, C12A7, CaS, C3A, and  $\text{MgO}\cdot\text{Al}_2\text{O}_3$  spinel used for this study. The Raman bands identified for each phase in this work corresponds with what had been previously reported in literature within a range of  $\pm 5 \text{ cm}^{-1}$  (Cormier & Massiot, 2010; Malavergne et al., 2013; Neuville, Henderson, Torr ns-Mart n et al., 2013; Sahoo et al., 2017).

**Table 6. Raman shift or bands ( $\text{cm}^{-1}$ ) for the synthetic inclusion phases (Reprinted [adapted] under CC BY license from Paper IV   2020 Authors).**

Phase	Measured peaks [Raman shift, $\text{cm}^{-1}$ ]	Reference [Raman shift, $\text{cm}^{-1}$ ]	Reference
CaS	157–160 s, 200 m, 478 w	160 s, 185 m, 215 ( $\pm 15$ ), 485 ( $\pm 10$ ) w	(Malavergne et al., 2013)
CA	525 s, 549 m, 790 w	520–521 s, 545–547 m, 790–793 w	(Neuville et al., 2010; Torr�ns- Mart�n et al., 2013)
C12A7	517 s, 781 m, 314 m	312–333 m, 516–517 m, 772 m, 779 m	(Neuville et al., 2010; Torr�ns- Mart�n et al., 2013)
C3A	756 s, 508 m	756–757 s, 140–150 w, 506–508 m	(Neuville et al., 2010; Torr�ns- Mart�n et al., 2013)
$\text{MgO}\cdot\text{Al}_2\text{O}_3$	416 s, 674 m, 773 m	409–412 s, 767–772 m, 666–674 m, 312–313 m	(Sahoo et al., 2017)

<sup>s</sup> is strong Raman signal, <sup>m</sup> is a medium Raman signal, <sup>w</sup> is weak Raman signal.

The main Raman peaks or bands observed at  $525 \text{ cm}^{-1}$  for CA,  $508 \text{ cm}^{-1}$  attributable to C3A and  $517 \text{ cm}^{-1}$  for C12A7 have bridged oxygens in the Al–O–Al linkages or are associated with symmetric stretching of the Al–O bonds in  $\text{AlO}_4^{5-}$  groups (McMillan & Piriou, 1983; Torr ns-Mart n et al., 2013). Raman bands located at  $790 \text{ cm}^{-1}$  for CA,  $781 \text{ cm}^{-1}$  for C12A7, and  $756 \text{ cm}^{-1}$  for C3A are assigned to asymmetric stretching modes found in  $\text{AlO}_4^{5-}$  tetrahedra (McMillan & Piriou, 1983; Torr ns-Mart n et al., 2013). Therefore, for calcium-aluminate system characteristic vibration modes of the distinctive bonded framework, Al–O is used to distinguish the difference in phases. Based on the Raman spectroscopy measurements conducted on the phases, the  $12\text{CaO}\cdot 7\text{Al}_2\text{O}_3$  (C12A7) phase had the most intense Raman peak position at  $517 \text{ cm}^{-1}$  and is located within a Raman band

region of 510–520  $\text{cm}^{-1}$ . Tricalcium aluminate (C3A) has the most identifiable and most intense Raman band position at 756  $\text{cm}^{-1}$ , with a medium Raman peak at 508  $\text{cm}^{-1}$ . Additionally, monocalcium aluminate (CA) has its most intense Raman peak at 525  $\text{cm}^{-1}$  and peak shoulder in the 545–549  $\text{cm}^{-1}$  region and with a weak Raman peak at 790  $\text{cm}^{-1}$ .

Raman bands observed at 416  $\text{cm}^{-1}$  for  $\text{MgO}\cdot\text{Al}_2\text{O}_3$  spinel is associated with a bending mode of Al ions located in tetrahedral sites, and for 674  $\text{cm}^{-1}$  they are linked to bands due to the bending motion that occurs in octahedral sites of Mg atoms (Dash et al., 2017). Additionally, a medium Raman band at 773  $\text{cm}^{-1}$  is a result of the symmetric stretching of the  $\text{AlO}_4$  in tetrahedral sites (Sahoo et al., 2017). The  $\text{MgO}\cdot\text{Al}_2\text{O}_3$  (MA) phase has its most intense Raman peak located at 416  $\text{cm}^{-1}$  and located within a region of 410–420  $\text{cm}^{-1}$ .

Figure 10 shows the Raman spectra measured from each specific phases used for preparing the sample mixtures for this study. For the CaS phase, the most intense Raman peak identified is found to be at 157  $\text{cm}^{-1}$  and with a medium peak around 200  $\text{cm}^{-1}$  and 478  $\text{cm}^{-1}$ .

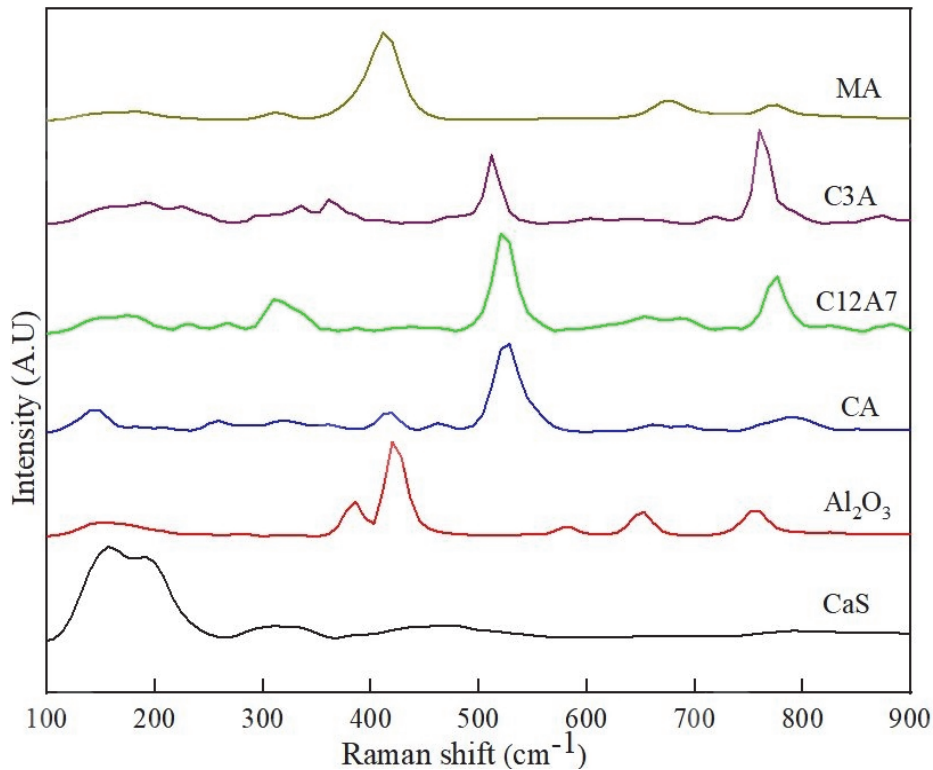


**Fig. 10.** Raman spectra for the synthetic phases of  $\text{MgO}\cdot\text{Al}_2\text{O}_3$  (MA), C3A, C12A7, CA,  $\text{Al}_2\text{O}_3$  and CaS (Reprinted [adapted] under CC BY license from Paper IV © 2020 Authors).

#### **4.2.1 Raman spectral observations based on the phases studied**

The ability to observe the Raman peak (bands) characteristic of a constituent in a sample measured using Raman spectroscopy provides first-hand information to consider if this type of vibrational spectroscopic system can be a robust characterisation technique. For this reason, a qualitative analysis was conducted by relating the specific phase (C12A7, C3A, CA, CaS or  $\text{MgO}\cdot\text{Al}_2\text{O}_3$ ) variation for a set of sample mixture with the change in the relative Raman peak intensity. Figures 11–13 illustrate how the observations made based on varying the individual phases content in a sample can affect the relative Raman peak (band) intensity.

*Sample mixtures that consist of C12A7, CA, C3A and MgO.Al<sub>2</sub>O<sub>3</sub>*

Figure 11 shows the Raman spectra for samples that contain C12A7 and C3A in a binary system with varying phase content. In Figure 11, an increment in the C12A7 phase content causes a corresponding rise in the peak intensities at the Raman band region of 510–520 cm<sup>-1</sup>. A similar trend can also be noticed for a change in the phase component for C3A (an increase or decrease) in C12A7-C3A had the corresponding effect on Raman region of 750–760 cm<sup>-1</sup>. These patterns observed in C12A7-C3A demonstrates that a variation in most intense Raman peak at 756 cm<sup>-1</sup> for C3A, relative to the most intense Raman peak 517 cm<sup>-1</sup> for C12A7 can be associated with the change in the sample phase content.

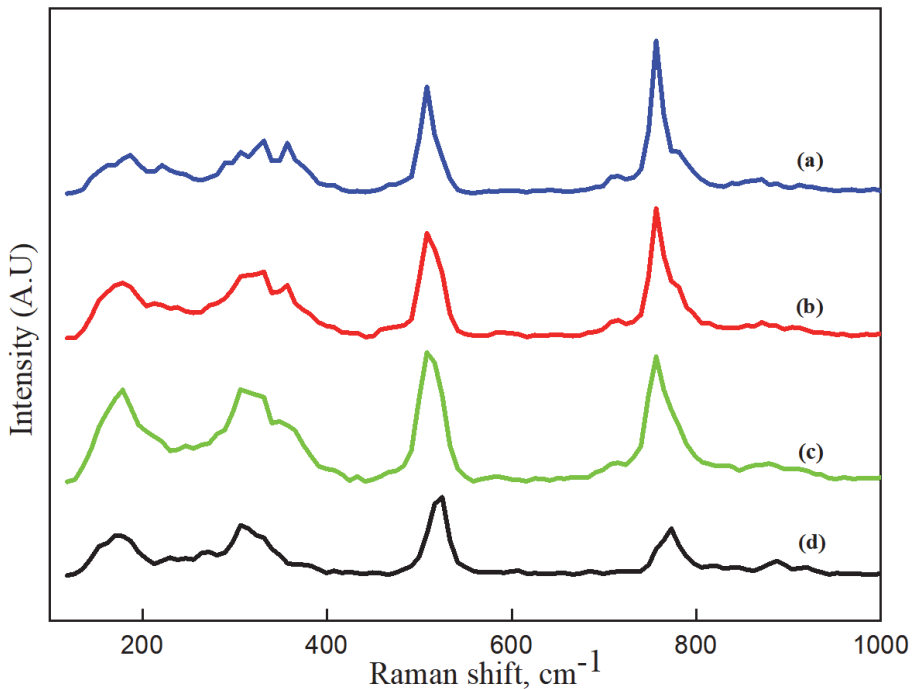


**Fig. 11. Raman spectra for the binary C12A7-C3A phase sample: (a) 20% of C12A7, (b) 40% of C12A7, (c) 50% of C12A7, and (d) 80% of C12A7 phase fraction (Reprinted [adapted] with permission from Paper I © 2019 ISIJ).**

For the MA phase content, it can be observed in Figure 12 that varying the MA phase content in the sample (C12A7-MA) has a corresponding effect in the Raman shift region of 410–420 cm<sup>-1</sup>. An increment in the phase content for MA also

demonstrates a corresponding rise in the most intense Raman peak at  $416\text{ cm}^{-1}$ , a characteristic feature of the MA phase. A similar observation could be made for the change in C12A7 content in the binary sample consisting of C12A7 and MA (C12A7-MA) at the most intense Raman peak found in the Raman band region of  $510\text{--}520\text{ cm}^{-1}$ .

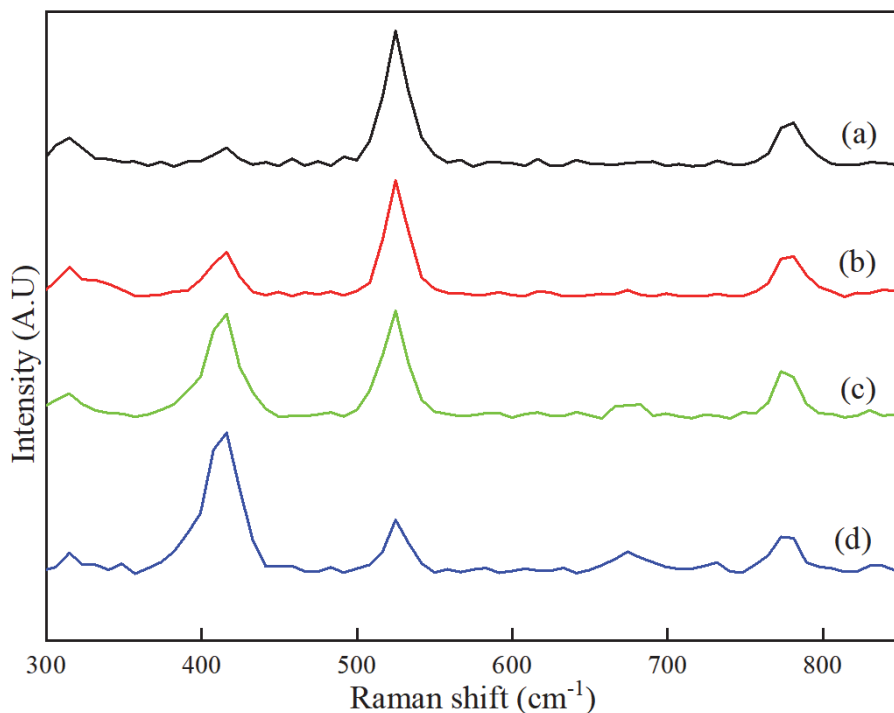


**Fig. 12.** Raman spectra for a binary C12A7-MA phase sample: MA content (a) 20 wt%, (b) 40 wt%, (c) 60 wt% and (d) 80 wt% (Reprinted [adapted] with permission from Paper II © 2020 ISIJ).

### *Raman spectral observation for CaS phase*

The ability to qualitatively estimate the phase content of CaS in a complex system such as  $\text{CaS}-(\text{Al}_2\text{O}_3-\text{CaO})-\text{MgO}.\text{Al}_2\text{O}_3$  using Raman spectroscopy can contribute and provide initial information for inclusion studies. Figure 13 is used to qualitatively show how the relative intensity of the Raman bands unique to a specific phase can be used to observe the phase content change in a ternary sample

system (MA–C12A7–CaS). Observations concerning the CaS phase in the MA–C12A7–CaS system show an increment in the phase content for CaS exhibits a rising Raman peak intensity in the region of 157–162  $\text{cm}^{-1}$ . This increase in intensity within the Raman band region (157–162  $\text{cm}^{-1}$ ) relates to the most intense Raman peak of CaS located at around 157  $\text{cm}^{-1}$ . Similarly, varying C12A7 and MgO. $\text{Al}_2\text{O}_3$  constituents in the MA–C12A7–CaS ternary system all had their most intense Raman bands (at 517  $\text{cm}^{-1}$  for C12A7 and 416  $\text{cm}^{-1}$  for MgO. $\text{Al}_2\text{O}_3$ ) intensity which also changed corresponding to the phase content in the samples (MA–C12A7–CaS), as discussed in the previous sections.

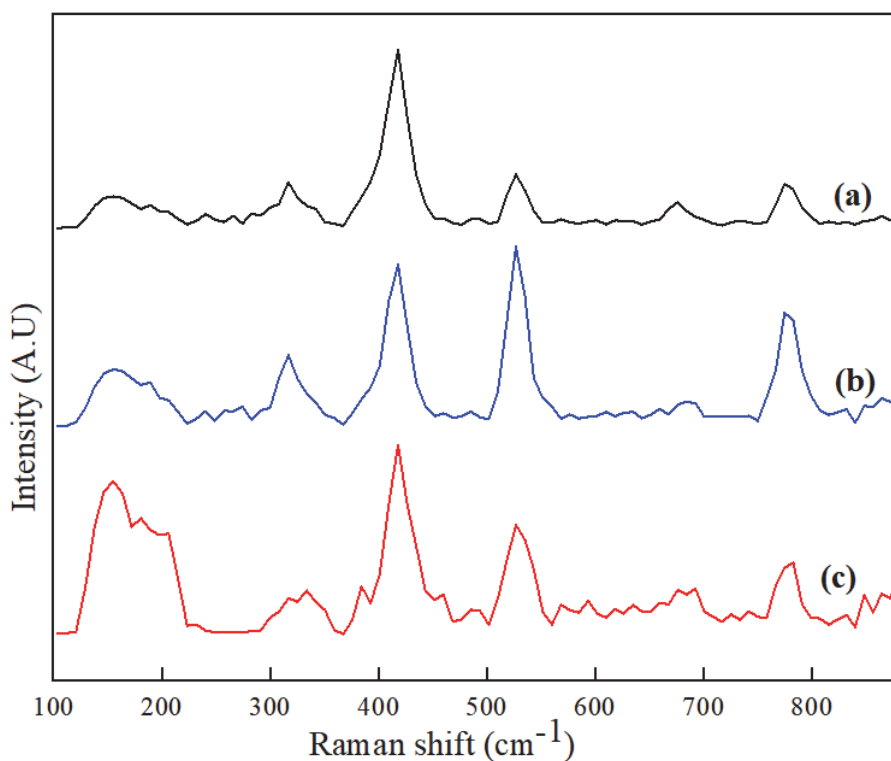


**Fig. 13.** Raman spectra of MA–C12A7–CaS ternary samples: (a) 70MA–20C12A7–10CaS, (b) 35MA–45C12A7–20CaS, and (c) 45MA–10C12A7–45CaS. Phase compositions given in wt% (Reprinted [adapted] with permission from Paper V © 2020 Wiley-VCH).

### 4.3 Phase quantification based on Raman spectral data

For quantitative evaluation, Tables 7–12 present the estimated statistical assessment parameter values, such as the mean absolute error (MAE), root mean standard error in calibration (RMSEC), root mean standard error in cross-validation (RMSECV), and coefficient of determination ( $R^2$ ). Figures 14–15 illustrate the estimated MAE, the relative stabilities ( $S_i$ ), the ratio of prediction to deviation (RPD), and the range error ratio (RER) of the calibration model. The most stable calibration variable candidate should have the highest degree of accuracy and repeatability based on the figure of merits.

#### 4.3.1 Calcium aluminate phases

The most desirable calcium aluminate inclusion is C12A7 since it is fully liquid under casting temperatures. On the other hand, other calcium aluminate phases of CA and C3A which can be formed in an attempt to achieve C12A7 under steel making conditions. The potential of forming CA and C3A along with C12A7 could depend on Ca addition in Al-killed steels and the activity of Al. Table 7 illustrates the coefficient of determination and the mean absolute error (MAE) values for Raman band ratio based on evaluating C12A7, C3A and CA content in the binary samples (C12A7-C3A and C12A7-CA). The Raman band ratio for 517/508 was estimated to have the best figure of merits compared to other peaks ratio in Table 7 for C12A7-C3A samples. However, for Raman spectroscopy to be used for both qualitative and quantitative estimation, it is recommended that the Raman band ratio of 517/756 is used as it has the second most promising values. Additionally, these Raman peaks are the most intense for C12A7 at 517  $\text{cm}^{-1}$  and C3A at 756  $\text{cm}^{-1}$  with fewer possibilities of peak overlap.

**Table 7. Evaluation of the coefficient of determination ( $R^2$ ) and mean absolute error (MAE) of the prediction and validation between the relative intensity of the Raman peaks and measured phase fraction for C12A7-C3A and C12A7-CA samples (Reprinted [adapted] with permission from Paper I © 2019 ISIJ).**

Phases	Relative intensity	Training data		Validation (ExVal)		Relative Stability
		Mean ( $R^2$ )	Mean (MAE)	Mean ( $R^2$ )	Mean (MAE)	
C12A7-C3A	517/508	0.97	2.69	0.97	3.04	0.32
	517/756	0.96	2.94	0.96	3.31	0.27
	314/756	0.94	3.67	0.93	3.78	0.16
	314/508	0.92	4.02	0.91	4.26	0.12
	781/756	0.91	4.74	0.93	5.22	0.09
	781/508	0.83	6.46	0.85	6.87	0.05
C12A7-CA	314/549	0.97	2.52	0.97	2.70	0.27
	314/522	0.94	3.69	0.93	3.93	0.18
	314/790	0.92	4.14	0.90	4.41	0.11
	517/522	0.88	4.46	0.88	5.09	0.09
	517/549	0.84	5.64	0.82	6.09	0.08
	517/790	0.86	5.70	0.87	6.24	0.06
	781/549	0.95	3.19	0.94	3.34	0.20
	781/522	0.45	11.12	0.43	12.20	0.00
781/790	0.03	14.41	0.17	15.51	0.01	

To quantify the C12A7 content in C12A7-CA samples, the relative Raman intensity ratio (314/549), where 314  $\text{cm}^{-1}$  is for C12A7 and 549  $\text{cm}^{-1}$  is for CA, gave the best coefficient of determination and had relatively the smallest mean absolute error values as presented in Table 7. The stability analysis from the studies also suggested that the Raman peak ratio of 314/549 for estimating C12A7 or CA phase content in C12A7-CA samples gave relatively the best figures of merits compared to others.

Furthermore, for a C12A7-CA binary system, Raman bands at 314  $\text{cm}^{-1}$  (a characteristic feature for C12A7) and 549  $\text{cm}^{-1}$  (attributable to the CA phase) are farther away from each other than 517  $\text{cm}^{-1}$  and 525  $\text{cm}^{-1}$ , and therefore there is less possibility of overlapping. Consequently, from the study, it is suggested that medium peaks should be used to distinguish phases in C12A7-CA samples since there is the possibility of peak overlap to occur at the most intense Raman peaks for C12A7 at 517  $\text{cm}^{-1}$  and for CA at 525  $\text{cm}^{-1}$ .

### 4.3.2 Calcium aluminate – $MgO \cdot Al_2O_3$ sample mixtures

The target towards steel cleanliness may encounter operational and control complexity, for example, the presence of elements such as Mg in the steel melt. The formation of both  $MgO \cdot Al_2O_3$  and calcium aluminate inclusions, such as C12A7, C3A and CA, are possible to be found in steel samples containing inclusion. Furthermore, the use of calcium treatment to modify  $Al_2O_3$  and spinel contribute to the formation of inclusions that exist in a  $MgO-Al_2O_3-CaO$  ternary system (Seo et al., 2010; Yang et al., 2011; Verma et al., 2012; Jiang et al., 2013; Tabatabaei et al., 2018). The researchers have demonstrated how relevant the  $MgO-Al_2O_3-CaO$  ternary system is to inclusion studies. The results presented and discussed in this section examine how to quantify a synthetic inclusion mixture consisting of  $MgO \cdot Al_2O_3$ , C12A7, C3A and CA using Raman spectroscopy.

The results here are inclusion systems that contain an  $MgO \cdot Al_2O_3$  (MA) spinel phase enveloped with calcium aluminate phases, such as CA, C12A7, C3A (Yang et al. 2012 and Deng et al. 2013). Table 8 (a–c) shows a binary system for C12A7-MA, C3A-MA and CA-MA for evaluating MA content in an MA–calcium aluminate (CA, C12A7 and C3A) system. The performance parameters of MAE and  $R^2$  show that the Raman peak intensity ratio of 517/416 had the best values for samples containing C12A7-MA, as shown in Table 8 (a). Similarly, for C3A-MA samples, the ratio of the peak intensities of Raman bands at 416  $cm^{-1}$  for MA and 756  $cm^{-1}$  for C3A produce the best  $R^2$  and the lowest MAE values, as demonstrated in Table 8 (b). Figure 14 shows a graphical representation for the estimated mean absolute error values and the relative stabilities for C3A-MA samples.

Additionally, in Table 8 (c), for samples consisting of CA and MA in CA-MA samples, the Raman band with the relative intensity ratio with better a mean absolute error and the highest linear regression coefficient of determination was 416  $cm^{-1}$  for MA and 522  $cm^{-1}$  for CA. Consequently, based on this study, it can be concluded that the most intense Raman peaks for the phases at 416  $cm^{-1}$  for MA, 756  $cm^{-1}$  for C3A, 517  $cm^{-1}$  for C12A7, and 522  $cm^{-1}$  for CA are the most suitable for the quantitative estimation of  $(CaO-Al_2O_3)$ -MA binary samples.

**Table 8. Estimation of the coefficient of determination ( $R^2$ ) and mean absolute error (MAE) of the prediction and validation between the relative intensity of the peaks and phase content for MA in calcium aluminate (CA, C12A7 and C3A)–MgO.Al<sub>2</sub>O<sub>3</sub> (MA) system (Reprinted [adapted] with permission from Paper II © 2020 ISIJ).**

Phases	Relative intensity	Training data		Validation		Relative Stability	Sum (MAE)
		Mean ( $R^2$ )	Mean (MAE)	Mean ( $R^2$ )	Mean (MAE)		
a: C12A7-MA	517/416	0.99	0.08	0.99	0.08	0.71	0.16
	517/674	0.86	0.31	0.87	0.32	0.05	0.63
	781/416	0.96	0.17	0.96	0.18	0.18	0.35
	781/674	0.91	0.25	0.91	0.26	0.06	0.51
b: C3A-MA	756/416	0.98	0.13	0.98	0.15	0.52	0.28
	508/416	0.97	0.13	0.97	0.14	0.40	0.27
	756/674	0.72	0.44	0.77	0.49	0.04	0.93
	508/674	0.67	0.47	0.78	0.54	0.03	1.01
c: CA-MA	522/416	0.97	0.13	0.97	0.15	0.60	0.28
	549/416	0.92	0.21	0.92	0.23	0.20	0.44
	522/674	0.73	0.44	0.77	0.47	0.09	0.91
	549/674	0.85	0.28	0.85	0.29	0.10	0.57

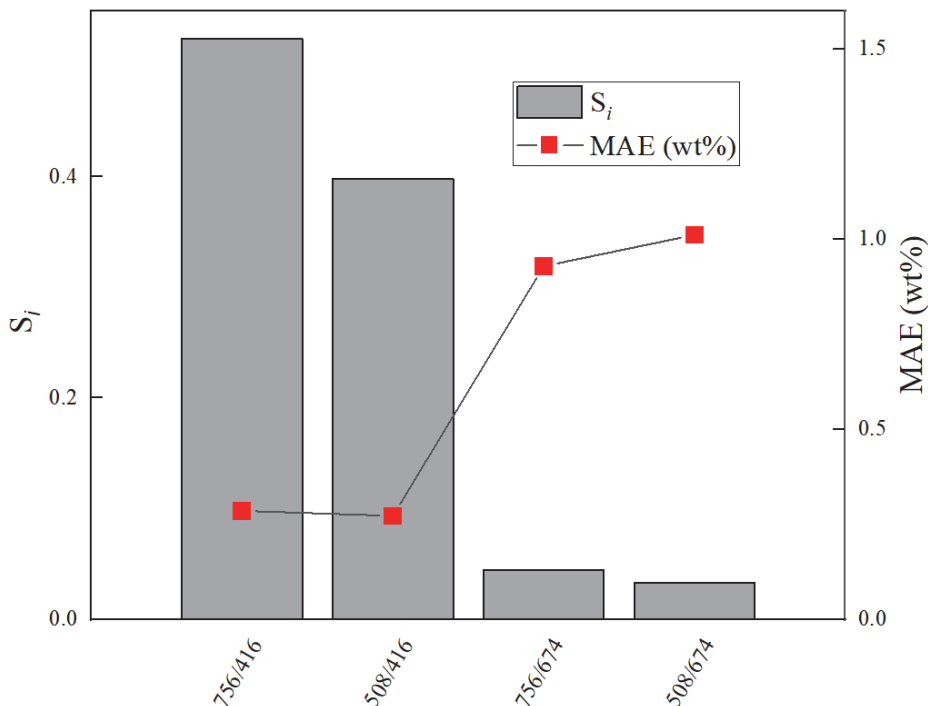


**Fig. 14. Estimation for relative stabilities ( $S_i$ ) of the calibration variable candidates and mean absolute error values for training and validation sets for C3A-MA (Reprinted [adapted] with permission from Paper II © 2020 ISIJ).**

Table 9 shows the figures of merits for estimating the individual phase fraction (CA, C12A7, C3A, MA) in the MgO–Al<sub>2</sub>O<sub>3</sub>–CaO ternary system. Table 9 illustrates MAE that ranges between 2.31 to 3.75 wt%, and with  $R^2$  ranging between 0.96–0.97 when a normalisation method is used for treating the Raman spectral data. However, it is worth indicating that the figures of merit without normalisation for the C12A7 phase gives  $R^2 = 0.6$  and MAE = 9.6 wt% for the external dataset. Therefore, for optimum calibration model performance for these set of samples, it is recommended to normalise the Raman spectral data.

**Table 9. Figures of merit for each of the calibration models measured with different data splits (Under CC BY license from Paper III © 2020 Authors).**

Phase	$R^2_t$	MAE <sub>t</sub>	$R^2_{iv}$	MAE <sub>iv</sub>	$R^2_{ev}$	MAE <sub>ev</sub>	n <sub>f</sub>	n <sub>l</sub>
C12A7	0.93	2.76	0.96	3.77	0.96	3.44	5	5
C3A	0.96	2.63	0.96	3.54	0.97	3.07	6	4
MA	0.97	3.13	0.99	2.31	0.97	2.31	15	10
CA	0.96	2.62	0.96	2.72	0.96	3.75	10	9

$t$  = training set,  $iv$  = internal validation set,  $ev$  = external validation set,  $f$  = features,  $l$  = latent features.

### 4.3.3 Calcium aluminate – MgO·Al<sub>2</sub>O<sub>3</sub> – CaS system

The formation of both MgO·Al<sub>2</sub>O<sub>3</sub> and CaS, along with calcium aluminate inclusions such as C12A7, C3A and CA, can be attributable to a high amount of sulphur or Mg in the steel melt, and operational challenges such as ineffective calcium treatment process. The results presented in this section examine how to quantify duplex oxide-sulphide and a ternary system of synthetic inclusion mixture consisting of C12A7, C3A, CA, MgO·Al<sub>2</sub>O<sub>3</sub> and CaS using Raman spectroscopy combined with calibration models.

The model performance assessment features, such as the coefficient of determination ( $R^2$ ), mean absolute error (MAE) and relative stabilities ( $S_i$ ), all demonstrate that the most intense Raman peak ratios are most suitable for estimating the individual phase fraction in the binary samples. The results for the C12A7-CaS samples are presented in Table 10 (a), where the most intense Raman peak ratio of 517/157 (C12A7/CaS) demonstrated to be the best candidates for evaluating samples that contain only CaS and C12A7. Similarly, in Table 10 (b), the CaS-C3A samples had the suitable Raman peak ratio of 766/157, having the best  $R^2$ , MAE, and  $S_i$  values suitable for evaluating the phase content in the CaS-C3A binary system.

For CA-CaS samples, Table 10 (c) further shows that the best figure of merits is the relative Raman peak intensity ratio of 157/524, where 157 cm<sup>-1</sup> is attributable to CaS and 524 cm<sup>-1</sup> is for CA phase constituents in the sample. Therefore, to evaluate the specific phase content in the CA-CaS samples, the most intense peaks for CaS and CA should be considered in the analysis of this type of sample. Consequently, the most intense Raman peaks for CaS, C12A7, C3A, and CA can be used for the quantitative estimation of individual phases in the samples studied.

**Table 10. Evaluation of the coefficient of determination ( $R^2$ ) and mean absolute error (MAE) for the prediction and validation between the phase content and relative intensity of the Raman peaks and phase content for CaS-(C12A7, C3A and CA) binary samples (Reprinted [adapted] under CC BY licence from Paper IV © 2020 Authors).**

Phases	Relative intensity	Training data		Validation		Sum (MAE)	Relative Stability
		Mean ( $R^2$ )	Mean (MAE)	Mean ( $R^2$ )	Mean (MAE)		
a: C12A7-CaS	517/157	0.98	2.76	0.98	2.96	5.72	0.98
	517/200	0.84	8.03	0.84	8.72	16.75	4.44
	781/157	0.90	6.06	0.90	6.43	12.49	1.54
	781/200	0.75	10.49	0.72	11.31	21.80	3.78
b: C3A-CaS	510/157	0.96	4.03	0.97	4.07	8.10	0.67
	766/157	0.88	6.50	0.88	6.92	13.42	0.09
	510/190	0.87	7.72	0.86	8.74	16.46	0.16
	766/190	0.85	8.07	0.82	8.97	17.04	0.08
c: CaS-CA	157/524	0.97	3.49	0.98	3.71	7.20	0.48
	157/790	0.92	6.08	0.93	6.12	12.20	0.15
	200/524	0.94	5.30	0.94	5.50	10.80	0.17
	200/790	0.83	9.27	0.84	9.49	18.76	0.07

This study further examines how to estimate the phase content of CA, C12A7, C3A, CaS and MgO.Al<sub>2</sub>O<sub>3</sub> spinel (MA) in a MgO.Al<sub>2</sub>O<sub>3</sub>-CaS-(CaO-Al<sub>2</sub>O<sub>3</sub>) ternary system by using a multivariate technique such as a PLS regression model. Five ternary samples of MA-C12A7-CaS, C12A7-CaS-CA, MA-CA-CaS, C12A7-CaS-C3A and MA-C3A-CaS were studied. The coefficient of determination ( $R^2$ ), root mean standard error in calibration (RMSEC), root mean standard error in cross-validation (RMSECV), and root mean square error of prediction (RMSEP) were the statistical parameters used for assessing calibration model performance, which are presented in Table 11. The average  $R^2$ , RMSEC, RMSECV and RMSEP values for pre-processed Raman data using standard normal variate (SNV) performed relatively very well compared to the raw Raman spectral data for the calibration model, as illustrated in Table 11.

**Table 11. The average figures of merit values for calibration and validation based on the PLS models for estimating C12A7, C3A, CaS, CA and MA from a MgO.Al<sub>2</sub>O<sub>3</sub>-CaS-(CaO-Al<sub>2</sub>O<sub>3</sub>) ternary system (Paper V).**

Phase	Method	R <sup>2</sup> <sub>CAL</sub>	R <sup>2</sup> <sub>CV</sub>	R <sup>2</sup> <sub>PRED</sub>	RMSEC, (wt%)	RMSEC, (wt%)	RMSEP, (wt%)
C12A7	Raw Data	0.88	0.73	0.77	6.95	11.12	9.98
	SNV	0.99	0.95	0.99	1.70	3.82	2.00
C3A	Raw Data	0.95	0.83	0.81	4.54	9.83	9.41
	SNV	0.99	0.93	0.97	1.79	5.04	3.48
CaS	Raw Data	0.86	0.75	0.77	8.02	12.35	11.19
	SNV	0.99	0.95	0.98	2.37	5.31	3.11
CA	Raw Data	0.71	0.56	0.66	13.26	16.46	15.33
	SNV	0.99	0.95	0.98	3.06	6.13	4.02
MA	Raw Data	0.94	0.84	0.81	5.19	9.70	10.29
	SNV	0.98	0.95	0.97	2.35	4.98	4.00

To further enhance the reliability of the calibration model, validation assessment parameters, such as the ratio of prediction to deviation (RPD) and the range error ratio (RER), were used. Table 12 shows the average values for RPD and RER used for estimating the specified phases of C12A7, CA, C3A, CaS and MA in the ternary samples studied in Paper V. Figure 15 (a) and (b) illustrates a bar chart demonstrating the performance of each phase based on the calibration model. In Figure 15 (a) and (b), when the bars assigned to each specific phase component in the sample mixture are equal or exceed the horizontal dotted line (red ink), this shows that the phase can be predicted satisfactorily based on the RPD (Figure 15(a))

and RER (Figure 15(b)) values. Raman spectra data treated with SNV exhibit better figures of merit compared to raw Raman data. Consequently, the use of a multivariate technique such as the PLS regression model shows that pre-processing the Raman spectra data gives more enhanced statistical parameters for estimating individual phase content in a  $\text{MgO} \cdot \text{Al}_2\text{O}_3\text{--CaS--}(\text{CaO--Al}_2\text{O}_3)$  ternary system.

**Table 12. The average RDP and RER values for assessing the performance of the specific phases of C12A7, C3A, CaS, CA and MA in a  $\text{MgO} \cdot \text{Al}_2\text{O}_3\text{--CaS--}(\text{CaO--Al}_2\text{O}_3)$  ternary system (Paper V).**

Component (Phase)	Mean RDP values		Mean RER values	
	Raw	SNV	Raw	SNV
C12A7	2.57	9.56	10.76	36.82
CA	1.74	6.53	5.33	20.00
C3A	2.63	6.63	9.24	22.41
CaS	2.74	9.05	8.45	28.47
MA	3.16	6.31	9.99	21.25

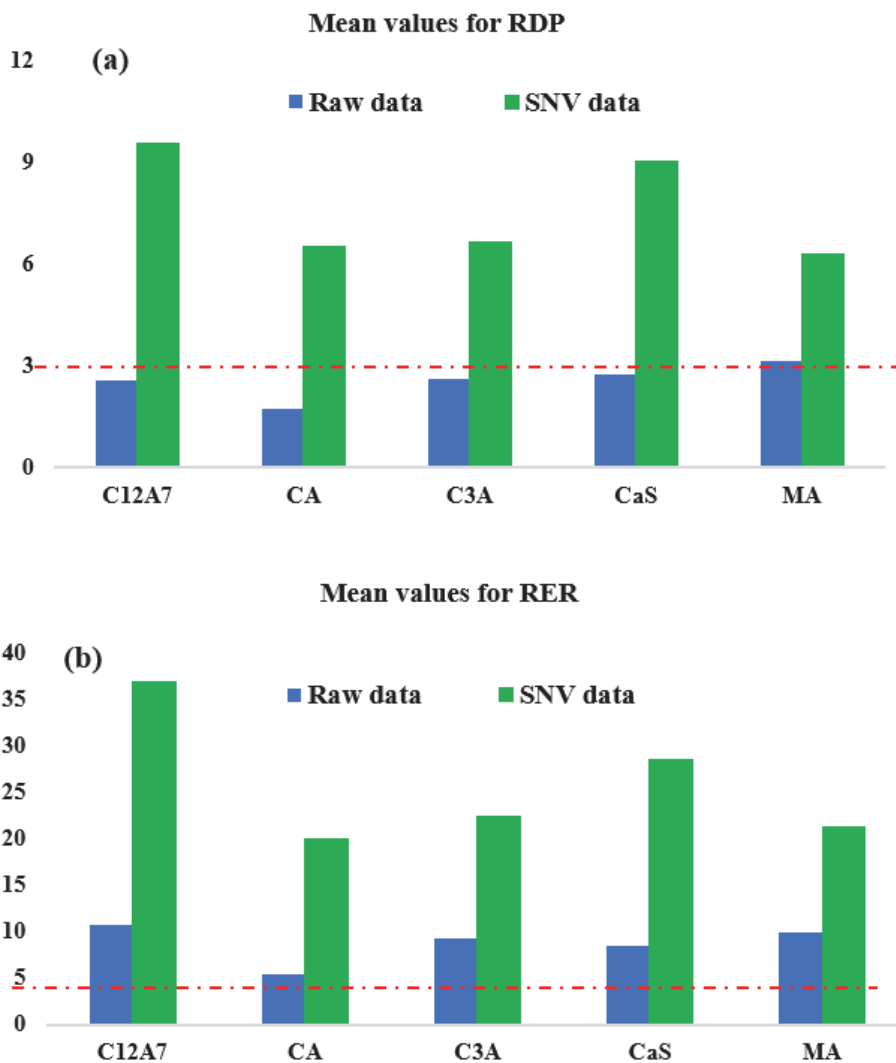


Fig. 15. Graphical chart of the data presented in Table 12 showing the performance for raw Raman data and SNV Raman data using (a) RDP and (b) RER values to estimate specific phases in a  $\text{MgO}\cdot\text{Al}_2\text{O}_3\text{-CaS-(CaO-Al}_2\text{O}_3)$  ternary system (Paper V).

#### 4.4 Prospect for application of Raman spectroscopy for steel samples studies

For the practical prospect of this study for non-metallic inclusions analysis in the steel samples, it is essential to consider the following parameters to ensure the effective utilisation of this study;

- *Sample features*: The samples (synthetic inclusions phases) used for this study could potentially have slight variation compared with actual steel samples relative to the inclusion size distribution and surface area. Non-metallic inclusions found within steel matrix are could generally be smaller in size and also in surface area compared to the samples used for this study.
- *Raman spectroscopy*: This technique (Raman spectroscopy) is generally considered as a surface phenomenon; therefore, it essential to take note for its application for inclusions with high depth within the steel matrix. Also, the laser beam focused on steel samples the during Raman measurement could generate Raman spectra containing numerous peaks for the Raman active composition of inclusions present in the sample. The prospect application for inclusion studies for steel samples to predict the presence of the phases analysed in this study can be identified based on the Raman peaks (bands) characteristic of the specific phase, as demonstrated from the studies conducted by Li & Hihara (2017).

The prospect of using vibrational spectroscopic techniques such as Raman spectroscopy for non-metallic inclusion based on this study can be explored for: 1) predicting liquidus region for a CaO–Al<sub>2</sub>O<sub>3</sub> binary system and 2) inclusion evolution, formation and steel cleanliness assessment.

##### 4.4.1 Liquidus region prediction

The general target for calcium treatment in Al-killed steel is to form calcium aluminate inclusion of C12A7 (12CaO.7Al<sub>2</sub>O<sub>3</sub>) due to its lowest liquidus temperature. Figure 16 illustrates FactSage<sup>TM</sup> software program used for estimating the stability areas for CA, C12A7 and C3A phases within the CaO–Al<sub>2</sub>O<sub>3</sub> system, and to show the liquidus region under steelmaking temperatures. From Figure 16, it could be predicted that the liquidus temperature of the calcium aluminate inclusions had exceeded the average casting temperature of approximately

1,520 °C considering that the CaO/Al<sub>2</sub>O<sub>3</sub> (weight ratio) is found outside the estimated range of 0.75–1.27.

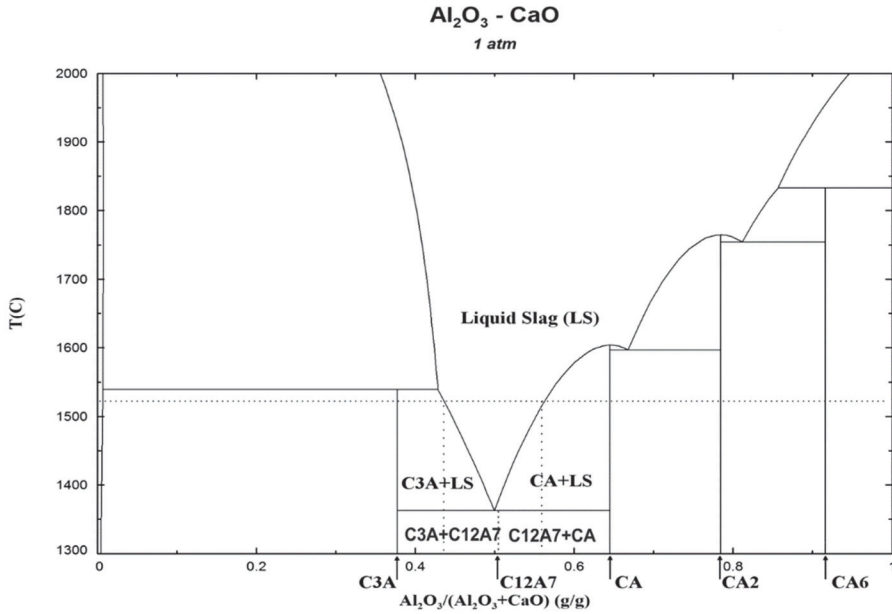


**Fig. 16. Phase diagram of the binary CaO–Al<sub>2</sub>O<sub>3</sub> system (Reprinted with permission from Paper I © 2019 ISIJ).**

For a C12A7-C3A system, when Raman spectral analysis indicates that the weight ratio of CaO/Al<sub>2</sub>O<sub>3</sub> is above  $1.79 \pm 0.07$ , the calcium aluminate inclusions would be solid in a casting temperature of 1,520 °C. Similarly, for a C12A7-CA binary system, if the weight ratio of CaO/Al<sub>2</sub>O<sub>3</sub> is found to be below  $1.02 \pm 0.04$ , the Raman measurement and analysis could predict that calcium aluminate inclusions would be more solid under an average casting temperature of 1,520 °C. The accuracy for estimating the evolution of C12A7 to C3A phase had mean absolute errors of 2.97 percentage points. For the modification of C12A7 to CA, an estimated mean absolute error of 2.55 percentage points was reported. Therefore, to predict liquid calcium aluminate inclusions, taking into consideration the error associated with the weight ratio of CaO/Al<sub>2</sub>O<sub>3</sub>, the Raman peak ratio values should exceed values of 0.98 for C12A7-CA and relatively below 1.86 for C12A7-C3A.

#### **4.4.2 Predicting evolution and formation routes for non-metallic inclusions based on Raman spectroscopy**

The evolution and formation of inclusions could have various routes, such as  $\text{Al}_2\text{O}_3 \rightarrow \text{MgO}.\text{Al}_2\text{O}_3$ , (MA)  $\rightarrow \text{CaO}.\text{Al}_2\text{O}_3$  (CA)  $\rightarrow \text{MgO}.\text{Al}_2\text{O}_3\text{--CaS--}(\text{CaO--Al}_2\text{O}_3)$  have been demonstrated by various researchers (Seo et al., 2010; Yang et al., 2011; Verma et al., 2012; Jiang et al., 2013; Tabatabaei et al., 2018) and the Papers I – V used for this study (illustrated in Figure 9). Papers II and III demonstrate the routes for predicting the evolution and formation of inclusions for the multiphase composition of  $(\text{CaO})_x(\text{Al}_2\text{O}_3)_y\text{--MgO}.\text{Al}_2\text{O}_3$ . Raman spectroscopy used for identifying and quantifying the specific phases (C3A, C12A7, CA and MA) in the samples shows that the binary systems (as presented in Paper II) relatively had the best level of accuracy compared to the ternary system (Paper III).

For route containing duplex oxide-sulphide inclusions such as CaS-C12A7, CaS-CA, MA-CaS (Paper IV) and for  $(\text{CaO--Al}_2\text{O}_3)\text{--MgO}.\text{Al}_2\text{O}_3\text{--CaS}$  system (presented in Paper V), it was observed that binary systems also had a higher level of accuracy compared to the ternary system (MA-C12A7-CaS, C12A7-CaS-CA, MA-CA-CaS, C12A7-CaS-C3A and MA-C3A-CaS) in predicting the phases present in the samples. However, the use of algorithm such as standard normal variate (SNV) for pre-processing the Raman spectral data provides enhanced results for estimating specific phases in a ternary system (Paper V).

This study shows Raman spectroscopy as a very promising analytical technique for the characterisation of synthesised inclusion that consists of the low melting phase of C12A7, partial liquidus phase of C3A, and potentially detrimental phases of CA, CaS and  $\text{MgO}.\text{Al}_2\text{O}_3$ . Consequently, this offers a potential reference database for future inclusion analysis of steel samples concerning the use of Raman spectroscopy, and also as a continuation of widening the scope of the application of Raman spectroscopy for inclusion characterisation for steel samples since steel matrix is not Raman active.



## 5 Conclusions and future work

### 5.1 Conclusions

This study investigated the application of Raman spectroscopy as a potential characterisation technique for the study of non-metallic inclusions commonly associated with Al-killed treated with calcium steels.

The binary sample mixtures between the C12A7 and CA or C3A were analysed with Raman spectroscopy. The prediction of the most suitable CaO/Al<sub>2</sub>O<sub>3</sub> ratio that forms a mixture of C12A7-CA and C12A7-C3A within liquidus region in a CaO–Al<sub>2</sub>O<sub>3</sub> binary system was also investigated. C12A7 is the most desirable inclusion for Al-killed treated with calcium steels since it is fully liquid under steelmaking temperatures. Therefore, this study considered the two closest phases to C12A7 in a CaO–Al<sub>2</sub>O<sub>3</sub> binary system (CA and C3A).

Experimental measurements using binary systems were conducted to study the Raman spectra obtained from a mixture between calcium aluminates phases (C12A7, CA and C3A) and potential detrimental phases such as MgO·Al<sub>2</sub>O<sub>3</sub> (MA) and CaS. The binary samples consisted of (CaO–Al<sub>2</sub>O<sub>3</sub>)–MA and duplex oxide–sulphide (CaS). Based on the Raman spectra measured from the samples, observations were used to estimate the individual phase content qualitatively. A change in phase content in the samples had a corresponding effect on the Raman band (peak) intensity attributable to the specific phase that makes up the sample. Calibration models were utilised to quantify the individual phase content present in the samples prepared. Based on the performance from the figures of merits, such as the coefficient of determination, MAE, and relative stabilities, the most suitable Raman peak ratio was selected for estimating the phase fraction in the samples.

Further experimental measurement works were carried out to demonstrate the use of Raman spectroscopy to distinguish synthetic inclusion phases in a ternary sample system that consisted of CA, C12A7, C3A, CaS and MA. Robust multivariate techniques such as PCA and PLS regression were used for establishing the calibration models to assist in the identification and quantification of the individual phases present in the ternary samples. The study also demonstrated the relevance of applying pre-processing algorithms, such as standard normal variate (SNV) and successive projection algorithm (SPA) methods, to the raw Raman spectra data to enhance the calibration model for predicting specific phase content in the sample. Statistical assessment parameters, such as coefficient of

determination ( $R^2$ ), root mean standard error in calibration (RMSEC), root mean standard error in cross-validation (RMSECV), and root mean square error of prediction (RMSEP), were used to check the suitability of the calibration model. Furthermore, the range error ratio (RER) and the ratio of prediction to deviation (RPD) were used to verify the calibration model performance in predicting the constituents in the sample concentration.

All these statistical assessment parameters provided very satisfactory results which demonstrate that the calibration model was fit for purpose in this study. Based on the use of experimentally prepared synthetic inclusions phases used in the study, three potential routes associated with the evolution and formation of inclusions for Al-killed calcium treated steel were investigated: firstly, the modification process for fully or partially liquid inclusions of calcium aluminates, such as CA, C12A7 and C3A; secondly, calcium aluminates combined with CaS or MgO.Al<sub>2</sub>O<sub>3</sub>, and, finally, the existence of CaS, MgO.Al<sub>2</sub>O<sub>3</sub> and calcium aluminates (C12A7, CA and C3A) in a sample matrix.

The study identified the following Raman band (shift) regions to be the most suitable for estimating the specific phase present in multiphase (binary and ternary) mixtures of CaO–Al<sub>2</sub>O<sub>3</sub>, (CaO–Al<sub>2</sub>O<sub>3</sub>)–MgO.Al<sub>2</sub>O<sub>3</sub> (MA) and (CaO–Al<sub>2</sub>O<sub>3</sub>)–MgO.Al<sub>2</sub>O<sub>3</sub>–CaS system:

- C12A7: Intense Raman band at 517–522 cm<sup>-1</sup>, medium Raman band within 776–781 cm<sup>-1</sup> or at 314 cm<sup>-1</sup>.
- C3A: Intense Raman band within 756–766 cm<sup>-1</sup>, medium Raman band at 508 cm<sup>-1</sup>.
- CA: Intense Raman band within 522–530 cm<sup>-1</sup> and medium Raman band at 545–549 cm<sup>-1</sup>.
- CaS: Intense Raman band within 156–160 cm<sup>-1</sup>.
- MgO.Al<sub>2</sub>O<sub>3</sub> (MA): Intense Raman band within 410–420 cm<sup>-1</sup>.

The accuracy for estimating the individual phase content (CA, C12A7, C3A, MgO.Al<sub>2</sub>O<sub>3</sub> and CaS), contained in the samples were assessed based on weight percent (wt%) deviations. The mean absolute error (MAE) values (in wt%), for a specific phase present in the sample based on the systems studied (binary and ternary), are presented as:

A. Calcium aluminate (CaO–Al<sub>2</sub>O<sub>3</sub>) system

- C12A7 (2.74), CA (2.61) and C3A (2.86)

B. (CaO–Al<sub>2</sub>O<sub>3</sub>)–MgO·Al<sub>2</sub>O<sub>3</sub> system

- Binary: MA (0.14), C12A7 (0.08), CA (0.14) and C3A (0.13) Al<sub>2</sub>O<sub>3</sub> (0.19)
- Ternary: MA (2.58), C12A7 (3.32), CA (3.03) and C3A (3.08)

C. (CaO–Al<sub>2</sub>O<sub>3</sub>)–MgO·Al<sub>2</sub>O<sub>3</sub>–CaS system

- Binary; CaS (0.21), MA (0.16), C12A7 (0.38), CA (0.13) and C3A (0.17), and Al<sub>2</sub>O<sub>3</sub> (0.21).
- Ternary; MA (3.78), CaS (3.60), C12A7 (2.51), CA (4.40) and C3A (3.44).

## 5.2 Future work

Vibrational spectroscopy like Raman spectroscopy has some features such as relatively non-destructive, easy sample preparation and fast result acquisition as some merits in its application as an analytical technique. Additionally, the steel matrix is Raman inactive, making Raman signals obtained from steel samples considered to be associated with inclusion within the steel matrix. Consequently, these features make Raman spectroscopy a potential analytical instrument for non-metallic inclusion characterisation in steel samples.

Future work should, therefore, consider the application of Raman spectroscopy a step further to characterise laboratory or industrial steel samples since the synthetic inclusions used in this study have shown themselves to be identifiable and distinguishable from each other using this instrumental technique.

Additionally, the prospect of using Raman spectroscopy as potential online studies for inclusions should be studied. However, experimental measurements should first be conducted on these synthetic inclusions at a higher temperature. This will assist in determining any possible thermal, or background effects on the Raman signals from the samples measured since all the Raman spectroscopy measurements for this current were done at ambient temperature.



## List of references

- Abdelaziz, S., Megahed, G., El-Mahallawi, I., & Ahmed, H. (2009). Control of Ca addition for improved cleanness of low C, Al killed steel. *Ironmaking & Steelmaking*, 36(6), 432–441.
- Araújo, M. C. U., Saldanha, T. C. B., Galvão, R. K. H., Yoneyama, T., Chame, H. C., & Visani, V. (2001). The successive projections algorithm for variable selection in spectroscopic multi-component analysis. *Chemometrics and Intelligent Laboratory Systems*, 57(2), 65–73.
- Avril, C., Malavergne, V., Caracas, R., Zanda, B., Reynard, B., Charon, E., Bobocioiu, E., Brunet, F., Borensztajn, S., Pont, S., Tarrida, M., & Guyot, F. (2013). Raman spectroscopic properties and Raman identification of CaS-MgS-MnS-FeS-Cr<sub>2</sub>FeS<sub>4</sub> sulfides in meteorites and reduced sulfur-rich systems. *Meteoritics and Planetary Science*, 48(8), 1415–1426.
- Barnes, R. J., Dhanoa, M. S. & Lister S. J. (1989). Standard normal variate transformation and de-trending of near-infrared diffuse reflectance spectra. *Applied Spectroscopy*, 43 (5), 772–777.
- Baumann, K. (2003). Cross-validation as the objective function for variable-selection techniques. *TrAC Trends in Analytical Chemistry*, 22(6), 395–406.
- Baumann, K., & Stiefl, N. (2004). Validation tools for variable subset regression. *Journal of Computer-Aided Molecular Design*, 18, 549–562.
- Beattie, J. R., Glenn, J. V., Boulton, M. E., Stitt, A. W., & McGarvey, J. J. (2009). Effect of signal intensity normalisation on the multivariate analysis of spectral data in complex “real-world” datasets. *Journal of Raman Spectroscopy*, 40(4), 429–435.
- Brabie, V. (1996). Mechanism of reaction between refractory materials and aluminum deoxidised molten steel. *ISIJ International*, 36, S109–S112.
- Chase, B. (1994). A new generation of Raman instrumentation. *Applied Spectroscopy*, 48 (7), 14A–18A.
- Chen, G. J., He, S. P., Guo, Y. T., Shen, B. Yi, Zhao, S., & Wang, Q. (2015). Optimisation of calcium addition to high-strength low-alloy steels. *Journal of Iron and Steel Research International*, 22(7), 590–597.
- Cho, S. W., & Suito, H. (1994). Assessment of calcium-oxygen equilibrium in liquid iron. *ISIJ International*, 34(3), 265–269.
- Choudhary, S. K., & Ghosh, A. (2008). Thermodynamic evaluation of formation of oxide-sulfide duplex inclusions in steel. *ISIJ International*, 48(11), 1552–1559.
- Cicutti, C. E., Madías, J., & González, J. C. (1997). Control of microinclusions in calcium treated aluminium killed steels. *Ironmaking & Steelmaking*, 24(2), 155–159.
- Colthup, N. B., Daly, L. H., Wiberley, S. E. (1990). *Introduction to Infrared and Raman Spectroscopy*, (3rd ed.). Academic Press: New York.
- Cooper, C. A., Elliott, R., & Young, R. J. (2003). Investigation of the graphitic microstructure in flake and spheroidal cast irons using Raman spectroscopy, 8, 795–802.

- Dandeu, A., Humbert, B., Carteret, C., Muhr, H., Plasari, E., & Bossoutrot, J. M. (2006). Raman spectroscopy - A powerful tool for the quantitative determination of the composition of polymorph mixtures: Application to CaCO<sub>3</sub> polymorph mixtures. *Chemical Engineering and Technology*, 29(2), 221–225.
- Das, R. S., & Agrawal, Y. K. (2011). Raman spectroscopy: Recent advancements, techniques and applications. *Vibrational Spectroscopy*, 57(2), 163–176.
- Dash, S., Sahoo, R. K., Das, A., Bajpai, S., Debasish, D., & Singh, S. K. (2017). Synthesis of MgAl<sub>2</sub>O<sub>4</sub> spinel by thermal plasma and its synergetic structural study. *Journal of Alloys and Compounds*, 726, 1186–1194.
- de Almeida, M. R., Correa, D. N., Rocha, W. F. C., Scafi, F. J. O., & Poppi, R. J. (2013). Discrimination between authentic and counterfeit banknotes using Raman spectroscopy and PLS-DA with uncertainty estimation. *Microchemical Journal*, 109, 170–177.
- Deng, Z., Zhu, M., & Sichen, D. (2016). Effect of refractory on nonmetallic inclusions in Al-killed steel. *Metallurgical and Materials Transactions B: Process Metallurgy and Materials Processing Science*, 47(5), 3158–3167.
- Fandrich, R., Lungen, H. B., & Wuppermann C. D. (2008). Actual review on secondary metallurgy. *Metallurgical Research & Technology*, 105 (7-8), 364–374.
- Fernandes de Oliveira Penido, C. A., Pacheco, M. T. T., E. H., Lednev, I. K., & Silveira, L. (2016). Raman spectroscopy in forensic analysis: identification of cocaine and other illegal drugs of abuse. *Journal of Raman Spectroscopy*. 47, 28–38.
- Ferraro, J. R., Nakamoto, K., & Brown, C. W. (2003). *Introductory Raman Spectroscopy* (2nd ed.). Cambridge: Elsevier.
- Geladi, P., & Kowalski B. R. (1986). Partial least-squares regression: a tutorial. *Analytica Chimica Acta*, 186, 1–17.
- Gollapalli, V., Rao, M. B. V., Karamched, P. S., Borra, C. R., Roy, G. G., & Srirangam, P. (2018). Modification of oxide inclusions in calcium-treated Al-killed high sulphur steels. *Ironmaking & Steelmaking*, 46, 663–670.
- Grinberg, N., & Rodriguez, S. (2019). *Ewing's Analytical Instrumentation Handbook*, (4th ed.). Boca Raton: CRC Press.
- Guyon, I & Elisseeff, A. (2003). An introduction to variable and feature selection. *Journal of Machine Learning Research*, 3, 1157–1182.
- Göransson, M., & Jänsson, P. G. (2001). Ideas for process control of during steelmaking. *ISIJ International*, 41, S42–S46.
- Harris, D. C., & Bertolucci, M. D. (1978). Symmetry and spectroscopy: An introduction to vibrational and electronic spectroscopy. *Oxford University Press*, Michigan.
- Harrell, F., E. (2001). *Regression modeling strategies*. Cham: Springer, 568, New York.
- He, S., Chen, G., Guo, Y., Shen, B., & Wang, Q. (2015). Morphology control for Al<sub>2</sub>O<sub>3</sub> inclusion without Ca treatment in high-aluminum steel. *Metallurgical and Materials Transactions B: Process Metallurgy and Materials Processing Science*, 46(2), 585–594.
- Heinz, A., Savolainen, M., Rades, T., & Strachan, C. J. (2007). Quantifying ternary mixtures of different solid-state forms of indomethacin by Raman and near-infrared spectroscopy. *European Journal of Pharmaceutical Sciences*, 32, 182–192.

- Hirlimann, C., Jouanne, M., & Forriès, C. (1992). Raman spectroscopy of graphite in cast iron. *Journal of Raman Spectroscopy*, 23, 315–317.
- Holappa, L. E. K., & Helle, A. S. (1995). Inclusion control in high-performance steels. *Journal of Materials Processing Technology*, 53, 177–186.
- Holappa, L. (2014). Secondary steelmaking. *Treatise on Process Metallurgy*, 3, 301–345.
- Jiang, Z., Zhuang, H. Y., Li, Y., & Li, S. J. (2013). Effect of modification treatment on inclusions in 430 stainless steel by Mg-Al alloys. *Journal of Iron and Steel Research International*, 20(5), 6–10.
- Jing, G., Shu-Sen, C., & Zi-Jian, C. (2013). Mechanism of non-metallic inclusion formation and modification and their deformation during compact strip production (CSP) process for aluminum-killed steel. *ISIJ International*, 53(12), 2142–2151.
- Kachrimanis, K., Braun, D. E., & Griesser, U. J. (2007). Quantitative analysis of paracetamol polymorphs in powder mixtures by FT-Raman spectroscopy and PLS regression. *Journal of Pharmaceutical and Biomedical Analysis*, 43, 407–412.
- Kawawa, T., Ohkubo, M. (1968). A kinetic study on deoxidation of steel. *ISIJ International*, 8(4), 203–219.
- Kiessling, R., & Lange, N. (1978). *Non-metallic inclusions in steel*, (2nd ed.). *Metals Society: London*.
- Kiessling, R. (1980). Clean steel- a debatable concept. *Metal Science Journal*, 15(5), 161–172.
- Li, S., & Hihara, L. H. (2017). Identification of inclusions in carbon steels using micro-Raman spectroscopy. *Journal Raman Spectroscopy*, 48, 137–142.
- Li, Y., Wan, X. L., Lu, W. Y., Shirzadi, A. A., Isayev, O., Hress, O., & Wu, K. M. (2016). Effect of Zr-Ti combined deoxidation on the microstructure and mechanical properties of high-strength low-alloy steels. *Materials Science and Engineering A*, 659, 179–187.
- Lis, T. (2009). Modification of oxygen and sulphur inclusions in steel by calcium treatment. *Metalurgija*, 48(2), 95–98.
- Lipiäinen, T., Pessi, J., Movahedi, P., Koivistoinen, J., Kurki, L., Tenhunen, M., Yliruusi, J., Juppo, A. M., Heikkonen, J., Pahikkala T., & Strachan, C. J. (2018). Time-gated Raman spectroscopy for quantitative determination of solid-state forms of fluorescent pharmaceuticals. *Analytical Chemistry*, 90(7), 4832–4839.
- McMillan, P., & Piriou, B., (1983). Raman spectroscopy of calcium aluminate glasses and crystals. *Journal of Non-Crystalline Solids*, 55(2), 221–242.
- McCreery, R. L. (2001). Raman spectroscopy for chemical analysis. *Measurement Science and Technology*, 12(5), 653.
- Miao, K., Haas, A., Sharma, K., Mu, W., Dogan, N. (2018). In situ observation of calcium aluminate inclusions dissolution into steelmaking slag. *Metallurgical and Materials Transactions B*, 49B, 1612–1623.
- Muñoz Tabares, J. A., & Anglada, M. J. (2010). Quantitative analysis of monoclinic phase in 3Y-TZP by Raman spectroscopy. *Journal of the American Ceramic Society*, 93(6), 1790–1795.

- Nadif, M., Lehmann, J., Burty, M., & Domgin, J. F. (2007). Control of steel reoxidation and CC nozzle clogging: An overview. *Revue de Metallurgie Cahiers D'Informations Techniques*, 104(10), 493–500.
- Neuville, D. R., Henderson, G. S., Cormier, L., & Massiot, D. (2010). The structure of crystals, glasses, and melts along the CaO-Al<sub>2</sub>O<sub>3</sub> join: Results from Raman, Al L- and K-edge X-ray absorption, and <sup>27</sup>Al NMR spectroscopy. *American Mineralogist*, 95(10), 1580–1589.
- Onoa, H., Mikib, T., & Hasegawac, M. (2014). Examples of steelmaking thermochemistry. *Treatise on Process Metallurgy*, 1, 617.
- Park, J. H., & Todoroki, H. (2010). Control of MgO.Al<sub>2</sub>O<sub>3</sub> spinel inclusions in stainless steels. *ISIJ International*, 50(10), 1333–1346.
- Park, J. S., Park, J. H. (2016). Effect of physicochemical properties of slag and flux on the removal rate of oxide inclusion from molten steel. *Metallurgical and Materials Transactions B*, 47(6), 3225–3230.
- Pires, J. C. S., & Garcia, A. (2004). Modification of oxide inclusions present in aluminum-killed low carbon steel by addition of calcium. *Rem: Revista Escola de Minas*, 57(3), 183–189.
- Poirier, J. (2015). A review: influence of refractories on steel quality. *Metallurgical Research & Technology*, 112(4), 410.
- Quentin, A. G., Rodemann, T., Doutreleau, M. F., Moreau, M., & Davies, N. W. (2017) Application of near-infrared spectroscopy for estimation of non-structural carbohydrates in foliar samples of Eucalyptus globulus Labillardière. *Tree Physiology*, 37, 131–141.
- Raman, C. V., & Krishnan, K. S. (1928). A new type of secondary radiation. *Nature*, 121(3048), 501–502.
- Sakata, K. (2006). Technology for production of austenite type clean stainless steel. *ISIJ International*, 46(12), 1795–1799.
- Seo, C. W., Kim, S. H., Jo, S. K., Suk, M. O., & Byun, S. M. (2010). Modification and minimisation of spinel (Al<sub>2</sub>O<sub>3</sub>• xMgO) inclusions formed in Ti-added steel melts. *Metallurgical and Materials Transactions B: Process Metallurgy and Materials Processing Science*, 41(4), 790–797.
- Saeys, W., Mouazen, A. M., Ramon, H. (2005). Potential for onsite and online analysis of pig manure using visible and near infrared reflectance spectroscopy. *Biosystems Engineering* 91(4), 393–402.
- Sahai, Y., & Emi, T. (2007). Tundish technology for clean steel production. *World Scientific Publishing*, Singapore.
- Singh, K. P., Basant, N., & Gupta, S. (2011). Support vector machines in water quality management. *Analytica Chimica Acta*, 703(2), 152–162.
- Smith, W. E., & Dent, G. (2005). Modern Raman Spectroscopy – A Practical Approach. *John Wiley & Sons, Ltd.*

- Sun, S., Waterfall, S., Strobl, N., Liao, D., & Holdridge, D. (2017) Inclusion control with Ca treatment to improve castability of low carbon aluminum-killed steel. *In Proceedings of the 8th International Symposium on High-Temperature Metallurgical Processing*, San Diego, CA, USA.
- Tabatabaei, Y., Coley, K. S., Irons, G. A., & Sun, S. (2018). Model of inclusion evolution during calcium treatment in the ladle furnace. *Metallurgical and Materials Transactions B*, 49(5), 375–387.
- Tabatabaei, Y., Coley, K. S., Irons, G. A., & Sun, S. (2018). A kinetic model for modification of  $MgAl_2O_4$  spinel inclusions during calcium treatment in the ladle furnace. *Metallurgical and Materials Transactions B: Process Metallurgy and Materials Processing Science*, 49(5), 2744–2756.
- Taguchi, K., Ono-Nakazato, H., Usui, T., Marukawa, K., Katogi, K., & Kosaka, H. (2005). Complex deoxidation equilibria of molten iron by aluminum and calcium. *ISIJ International*, 45(11), 1572–1576.
- Teixeira dos Santos C. A., Páscoa R. N. M. J., Porto, P. A. L. S., Cerdeira A. L., González-Sáiz, J. M., Pizarro, C., & Lopes, J. A. (2018). Raman spectroscopy for wine analyses: A comparison with near and mid infrared spectroscopy. *Talanta*, 186, 306–314.
- Thunman, M., & Sichen, D. (2008). Origins of non-metallic inclusions and their chemical development during ladle treatment. *Steel Research International*, 79(2), 124–132.
- Tian, Z. Q., Yang, Z. L., Ren, B., Li, J. F., Zhang, Y., Lin, X. F., & Wu, D. Y. (2006). Surface-enhanced Raman scattering from transition metals with special surface morphology and nanoparticle shape. *Faraday Discussions*, 132, 159–170.
- Torréns-Martín, D., Fernández-Carrasco, L., Martínez-Ramírez, S., Ibáñez, J., Artús, L., & Matschei, T. (2013). Raman spectroscopy of anhydrous and hydrated calcium aluminates and sulfoaluminates. *Journal of the American Ceramic Society*, 96(11), 3589–3595.
- Vankeirsbilck, T., Vercauteren, A., Baeyens, W., Van der Weken, G., Verpoort, F., Vergote, G., & Remon, J. P. (2002). Applications of Raman spectroscopy in pharmaceutical analysis. *Trends in Analytical Chemistry*, 21(12), 869–877.
- Verma, N., Pistorius, P. C., Fruehan, R. J., Potter, M. S., Oltmann, H. G., & Pretorius, E. B. (2012). Calcium modification of spinel inclusions in aluminum-killed steel: Reaction steps. *Metallurgical and Materials Transactions B: Process Metallurgy and Materials Processing Science*, 43(4), 830–840.
- Way, L. D. (2001). Cleaness, castability, and surface quality of formable sheet steels. *Materials Science and Technology*, 17(10), 1175–1190.
- Wold, S., Ruhe, A., Wold, H., and Dunn, W. J. III. (1984). The collinearity problem in linear regression. The partial least squares (PLS) approach to generalized inverses. *SIAM Journal on Scientific and Statistical Computing*, 5(3) 735–743.
- Xu, Z. Y., Liu, J. H., He, Z. J. & Pang, Q. H. (2018). Study on clogging mechanism of submerged entry nozzle of steel 38CrMoAl, *Metalurgija*, 57, 79–82.
- Yang, S. F., Li, J. S., Wang, Z. F., Li, J., & Lin, L. (2011). Modification of  $MgO \cdot Al_2O_3$  spinel inclusions in Al-killed steel by Ca-treatment. *International Journal of Minerals, Metallurgy and Materials*, 18(1), 18–23.

- Yan, P., Arnout, S., Van Ende, M., Zinngrebe, E., Jones, T., Blanpain, B., & Guo, M. (2015). Steel reoxidation by gunning mass and tundish slag. *Metallurgical and Materials Transactions B*, *46*, 1242–1251.
- Ye, G., Jönsson, P., & Lund, T. (1996). Thermodynamics and kinetics of the modification of Al<sub>2</sub>O<sub>3</sub> inclusions. *ISIJ International*, *36*, S105–S108.
- Zhao, D., Li, H., Bao, C., Yang, J. (2015). Inclusion evolution during modification of alumina inclusions by calcium in liquid steel and deformation during hot rolling process. *ISIJ International*, *55*(10), 2115–2124.
- Zhang, G. H., & Chou, K.-chih. (2015). Deoxidation of molten steel by aluminum. *Journal of Iron and Steel Research International*, *22*(10), 905–908.
- Zhang, L., & Thomas, B. G. (2003b). State of the art in evaluation and control of steel cleanliness. *ISIJ International*, *43*(3), 271–291.
- Zhang, L., & Thomas, B. G. (2006). State of the art in the control of inclusions during steel ingot casting. *Metallurgical and Materials Transactions B: Process Metallurgy and Materials Processing Science*, *37*(5), 733–761.

## Original publications

- I Gyakwaa, F., Aula, M., Alatarvas, T., Vuolio, T., Huttula, M., & Fabritius, T. (2019). Applicability of time-gated Raman spectroscopy in the characterisation of calcium-aluminate inclusions. *ISIJ International*, *59*(10), 1846–1852. doi: /10.2355/isijinternational.ISIJINT-2019-122
- II Gyakwaa, F., Aula, M., Alatarvas, T., Vuolio, T., Shu, Q., Huttula, M., & Fabritius, T. (2020). Characterisation of binary phase mixtures of magnesium-aluminate spinel and calcium-aluminates using time-gated Raman spectroscopy. *ISIJ International*, *60*(5), 988–997. doi: 10.2355/isijinternational.ISIJINT-2019-576
- III Gyakwaa, F., Aula, M., Vuolio, T., Alatarvas, T., Shu, Q., Huttula, M., & Fabritius, T. (2020). Characterisation of multiphase mixtures of calcium aluminates and magnesium aluminate spinel using time-gated Raman spectroscopy. *Steel Research International*, *91*(8), 2000084. doi: 10.1002/srin.202000084
- IV Gyakwaa, F., Aula, M., Alatarvas, T., Vuolio, T., Shu, Q., Huttula, M., & Fabritius, T. (2020). Application of Raman spectroscopy for characterising synthetic non-metallic inclusions consisting of calcium sulphide and oxides. *Applied Sciences*, *10*(6), 2113. doi:10.3390/app10062113
- V Gyakwaa, F., Aula, M., Alatarvas, T., Shu, Q., Huttula, M., & Fabritius, T. (2020). Quantification of synthetic nonmetallic inclusion multiphase mixtures from a CaO–Al<sub>2</sub>O<sub>3</sub>–MgO–CaS system using time-gated Raman spectroscopy. *Steel Research International*, 2000322. doi: 10.1002/srin.202000322

Reprinted with permission from ISIJ (Papers I and II), Wiley-VCH (Paper V), and under CC BY licence (Papers III and IV) from Authors and MDPI.

Original publications are not included in the electronic version of the dissertation.



744. Frondelius, Tero (2020) Development of methods in engine design process
745. Rissanen, Jouni (2020) Utilization of peat-wood fly ash from fluidized bed combustion as supplementary cementitious material
746. Särestöniemi, Mariella (2020) UWB in-body propagation and radio channel characteristics for wireless body area network applications
747. Ashraf, Faisal Bin (2020) River regimes and energy demand interactions in Nordic rivers
748. Kuula, Seppo (2020) Continuous co-creation of knowledge-intensive business services
749. Mustonen, Erno (2020) Vertical productisation over product lifecycle : co-marketing through a joint commercial product portfolio
750. Halttula, Heikki (2020) Enhancing data utilisation in the construction project lifecycle through early involvement and integration
751. Nguyen, Hoang (2020) Ettringite-based binder from ladle slag : from hydration to its fiber-reinforced composites
752. Jahromi, Sahba S. (2020) Single photon avalanche detector devices and circuits for miniaturized 3D imagers
753. Xu, Yingyue (2020) Computational modeling for visual attention analysis
754. Saarela, Martti (2020) Growth management of eHealth service start-ups
755. Kolli, Satish (2020) Sensitization in austenitic stainless steels : quantitative prediction considering multicomponent thermodynamic and mass balance effects
756. Ali, Mohammed (2020) Development of low-cost CrNiMoWMnV ultrahigh-strength steel with high impact toughness for advanced engineering applications
757. Khan, Hamza (2020) Resource scheduling and cell association in 5G-V2X
758. Miettinen, Jyrki & Visuri, Ville-Valtteri & Fabritius, Timo (2020) Chromium-, copper-, molybdenum-, and nickel-containing thermodynamic descriptions of the Fe–Al–Cr–Cu–Mn–Mo–Ni–Si system for modeling the solidification of steels
759. Alasalmi, Tuomo (2020) Uncertainty of classification on limited data
760. Kinnunen, Hannu (2020) Studies for the development, validation, and application of wearable technology in the assessment of human health-related behavior
761. Abou Zaki, Nizar (2020) The role of agriculture expansion in water resources depletion in central Iran

S E R I E S E D I T O R S

**A**  
**SCIENTIAE RERUM NATURALIUM**  
*University Lecturer Tuomo Glumoff*

**B**  
**HUMANIORA**  
*University Lecturer Santeri Palviainen*

**C**  
**TECHNICA**  
*Postdoctoral researcher Jani Peräntie*

**D**  
**MEDICA**  
*University Lecturer Anne Tuomisto*

**E**  
**SCIENTIAE RERUM SOCIALIUM**  
*University Lecturer Veli-Matti Ulvinen*

**E**  
**SCRIPTA ACADEMICA**  
*Planning Director Pertti Tikkanen*

**G**  
**OECONOMICA**  
*Professor Jari Juga*

**H**  
**ARCHITECTONICA**  
*University Lecturer Anu Soikkeli*

**EDITOR IN CHIEF**  
*University Lecturer Santeri Palviainen*

**PUBLICATIONS EDITOR**  
*Publications Editor Kirsti Nurkkala*

ISBN 978-952-62-2728-3 (Paperback)  
ISBN 978-952-62-2729-0 (PDF)  
ISSN 0355-3213 (Print)  
ISSN 1796-2226 (Online)